J. Fluid Mech. (2009), *vol.* 631, *pp.* 23–63.
doi:10.1017/S0022112009007009 Printed in the United Kingdom

An experimental study of an axisymmetric turbulent pulsed air jet

I. CHOUTAPALLI†‡, A. KROTHAPALLI AND J. H. ARAKERI¶

Department of Mechanical Engineering, 2525 Pottsdamer Street

Florida A&M University and Florida State University, Tallahassee, FL 32310, USA

(Received 23 October 2008 and in revised form 11 January 2009)

An experimental study is carried out to elucidate the structure of a high Reynolds number ($\sim 10^5$) turbulent pulsed jet. Particle image velocimetry measurements showed that the near flow field is dominated by a series of vortex rings with jet-like flows in between. The data show that the vortex rings convect at nearly constant speed of $0.6U_j$ (U_j: mean jet exit velocity) and the spacing between the rings assumes a value of about $0.6/St$ (St: Strouhal number $= fd/U_j$, where f is the pulsing frequency and d is the nozzle exit diameter). With increasing Strouhal number, the rings are closely spaced and the flow tends to assume a steady jet character at five diameters downstream of the nozzle exit. At lower Strouhal numbers there is a distinct region of jet flow in between the rings. Many of the global characteristics, entrainment, mass and momentum flux are essentially determined by the strength and spacing of the rings which, in turn, depend on St. We show that the increase in momentum is due to both increased momentum flux and overpressure at the exit in accordance with Krueger & Gharib (*AIAA J.*, vol. 43 (4), 2005, p. 792). This increase in momentum comes at the expense of higher energy required to produce the jet. We also present results of organized and random components of the fluctuations and production of the random turbulence in a pulsed jet. The two regions of dominant turbulence production are identified with the ring and the trailing jet shear layers.

1. Introduction

The first successful application of a pulsed jet engine was during the World War II for propelling a flying bomb (Manganiello, Valerino & Essig 1945). The advantage of such an engine is its extremely light weight obtained by simple construction. These engines are especially useful in relatively short duration operation at high speeds. As such pulsed jet engines have been of interest with applications varying from radio-controlled small aircraft to vertical take off and landing (VTOL) aircraft. Our interest here is the use of pulsed jet in a thrust augmenting ejector configuration to yield high levels of thrust augmentation to achieve short-duration vertical flight. In support of a number of previous investigations, a recent study (Choutapalli & Krothapalli 2009,

† Email address for correspondence: cisaac@tamu.edu

‡ Present address: Department of Nuclear Engineering, Texas A & M University, College Station, TX 77843-3133, USA

¶ Present address: Department of Mechanical Engineering, Indian Institute of Science, Bangalore, India

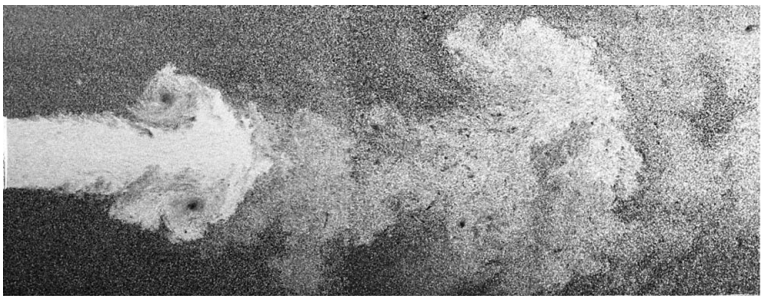

FIGURE 1. Flow visualization of a pulsed jet obtained from experimental apparatus described in § 2; $St = 0.11$; $U_j = 100.5\,\mathrm{m\,s^{-1}}$.

and references therein) suggests a possibility of achieving thrust augmentation ratio (total thrust/primary jet thrust) of about 2.3 if the primary jet is pulsed at a Strouhal number (fd/U_j; where f is the primary jet pulsing frequency, d is the primary nozzle exit diameter and U_j is the mean primary jet exit velocity) of about 0.25 using a compact ejector. Furthermore, it is found that the ejector performance is determined largely by the spatio-temporal evolution of the primary pulsed jet. With this in mind, an experimental investigation was carried out to provide an understanding of free pulsed jet structure and its dependence on the major parameters, such as the pulsing frequency, pulse characteristics and mean jet exit Mach number. For all the experiments considered here, the Reynolds number, based on the mean exit velocity and nozzle diameter, is sufficiently large enough to yield turbulent boundary layer at the nozzle exit. Although experiments were conducted at exit Mach numbers ranging from 0.1 to 0.8, and since compressibility was found to play only a secondary role in the jet evolution (Choutapalli 2006), for brevity, only the incompressible jet results will be presented here. Most of the previous investigations on pulsed jets simplified the flow to an isolated vortex ring created either by a piston driver at low velocities (Dabiri & Gharib 2004) or by a shock tube at impulsive supersonic conditions (Arakeri *et al.* 2004). The study of a continuously generated pulsed jet flow field at high Reynolds numbers received relatively little attention. Pulsed jets can be found in a variety of applications such as blood flow in a heart (Gharib *et al.* 2006), jets in cross-flows (M'Closkey *et al.* 2002 and Johari 2006), active flow control (Smith & Glezer 1998) and pulse detonation engines (PDEs). Additionally, several aquatic animal propulsive flows display characteristics that resemble a pulsed jet (Dabiri 2005). Crow & Champagne (1971) forced a moderate Reynolds number ($Re_d \sim 10^4$) axisymmetric jet, using a loudspeaker, to produce a jet with large-scale vortical structures that are commonly referred to as 'puffs' or 'vortex rings'. These structures are typically a manifestation of the Kelvin–Helmholtz instability in the shear layer and the forcing is primarily used to enhance the unstable mode of the jet. The exit velocity of the jet however remains relatively constant and the forcing is simply a perturbation. We refer to a pulsed jet as one in which variation with time of the exit velocity is large and of the same order of magnitude as the mean exit velocity. Even though the pulsed jet shows vortex rings similar to those of perturbed jets, they are much stronger (figure 1) resulting in a different jet, a description of which is the subject of this paper. The strongly pulsed jet is considered as that where the root mean square (r.m.s.) velocity is substantially greater than the time-average velocity at the nozzle and the slug of jet fluid associated with each pulse is relatively short generating a series of compact vortex rings.

One of the consequences of forcing is an increase in entrainment of the ambient fluid. For example, at a downstream location of four diameters, Crow & Champagne (1971) found an increase in the entrained volume flow of 32 % at a Strouhal number of 0.3. A much stronger forcing of the jet results in higher values of entrainment as demonstrated by Vermeulen, Ramesh & Wai (1986) and was found to be maximum at $St = 0.25$ with a higher entrained volume flow of about 150 %.

Bremhorst & Hollis (1990) and Bremhorst & Gehrke (2000) carried out studies on fully pulsed jets. In a fully pulsed jet, the jet velocity returns to zero between pulses for a finite amount of time. Bremhorst & Hollis (1990) examined a pulsed jet operating at $St = 0.007$. An increase of about 100 % in the mass entrainment as compared to a steady jet was observed. The experimental results show that vortex-dominated regions indicate large values of turbulence intensities. This flow may be treated as a series of vortex rings well separated in time similar to that of Krueger & Gharib (2005), who studied systematically the effects of pulsing duty cycle and the ratio of the ejected slug length (length of the fluid ejected out during a cycle) to diameter. Significant thrust augmentation by pulsing was observed as compared to steady jet with identical mass flux. The increased thrust is attributed to the overpressure at the nozzle exit plane during vortex ring formation and the increased momentum due to the unsteadiness. Low Strouhal number pulsed jets may be considered to be a series of non-interacting vortex rings. However, at high Strouhal numbers, the jet approaches to that of a 'steady jet'.

Siekmann (1963) has derived expressions for thrust produced by unsteady planar jets using control volume analysis in the context of aquatic propulsion by pulsed jets. The results of his analysis compares favourably with previously reported experimental data. In his study, Weihs (1977) used a periodic train of vortex rings to analyse the thrust produced by aquatic animals that use pulsed jet propulsion. It was shown that when the pulsing frequency is sufficiently high, the mutual interaction of the vortex rings could have substantial hydrodynamic and propulsive benefits.

Although substantial literature exists on turbulent jets, few experiments have been carried out on a pulsed jet with the degree of thoroughness found in either of the steady and perturbed jets. Majority of the studies on pulsed jets are conducted at relatively low Reynolds numbers and in most cases without clear description of the jet exit conditions. The important issues related to the pulsed jet development: the entrainment, thrust augmentation and turbulence are examined in our study using phase-locked particle image velocimetry (PIV). Additionally, the pulsed jet flow evolution is characterized in terms of its main components: vortex ring, the trailing and background jets. When appropriate a direct comparison of the pulsed jet and the corresponding steady jet is made.

In the present experiment, a pulsed jet results when the flow rate exiting a nozzle into still ambient varies cyclically in time. The main parameters that define the jet are the mean exit velocity ($U_j = \frac{8}{d^2 t} \int_0^{d/2} \int_0^t u(r,t)\, r\, \mathrm{d}r\, \mathrm{d}t$, where u is the instantaneous axial velocity, t is the time during a cycle and d is the nozzle exit diameter and the centre of the nozzle is defined as the origin), phase-averaged maximum velocity within a cycle($\langle u_c \rangle_{max}$: c.f. figure 4), phase-averaged minimum velocity within a cycle ($\langle u_c \rangle_{min}$: c.f. figure 4) and the r.m.s. value of the periodic axial velocity component ($\tilde{u}_{c,rms}$) at the centre of nozzle exit and the time period of pulsing ($\tau = 1/f$, where f is the pulse frequency). The profiles in time and profiles across the exit cross-section (e.g. top hat) of the phase-averaged velocity and phase-averaged turbulent velocities are additional parameters. The temporally and spatially averaged axial velocity at the nozzle exit plane is used as the mean jet velocity. A convenient set of non-dimensional

parameters are Reynolds number based on the mean exit velocity and the nozzle exit diameter ($Re_d = U_j d/\nu$), Strouhal number (fd/U_j or a non-dimensional time $T^* = U_j \tau/d = 1/St = L/d$), $\langle u_c \rangle_{max}/U_j$ and $\langle u_c \rangle_{min}/U_j$ and $\tilde{u}_{c,rms}/U_j$. We show below that T^* gives an immediate picture of the axial spacing of the structures and is preferable to the more commonly used Strouhal number.

A pulsed jet in the near field is perhaps best described as a series of vortex rings interspersed by jet-like flows. However, depending on the way the pulsed jet is produced, the jet flows between the rings may be absent. Such a jet occurs in the case of low frequency pulsing with long time interval of zero exit flow between the pulses (Bremhorst & Gehrke 2000). Many important global characteristics of a pulsed jet, such as entrainment and spreading rate, are determined by two main parameters: the spacing and strength of these vortex rings. The spacing Δx_{ring} is given by the product of the convection speed of the rings and the time period of pulsation $U_{ring}\tau$. As shown later, in the near field, $U_{ring} \approx 0.6U_j$; thus, $\Delta x_{ring}/d = 0.6U_j\tau/d = 0.6T^* = 0.6/St$. The relation $U_{ring} = 0.6U_j$ is valid only in the near field and only for some types of pulsed jets. But the relation $\Delta x_{ring} = U_{ring}\tau$ is valid at all downstream locations and for all types of pulsed jets. For example, when there is a large period of zero exit flow between pulses (low duty cycle), the ring convection velocity will be closer to some factor (<1) of the average exit velocity during the period when the flow is on. With downstream distance, the U_{ring} value is expected to decay as some function of x.

A brief explanation of the measurement set-up, data processing procedure and the parameter range is given in § 2. Recognizing that the initial conditions are important in determining the downstream evolution of the pulsed jet, in § 2.1, a description of these is delineated. In § 3.1, the evolution of the jet is described using the phase-averaged velocity and vorticity fields. The global mean and turbulence characteristics of the pulsed jet are compared with a steady jet in § 3.3. A summary of the observations is used to provide a basic understanding of the pulsed jet in § 4. In this paper, for brevity, we only use and report the data that are required to elucidate the salient features of a pulsed jet. For more detailed information, reference can be made to Choutapalli (2006).

2. Experimental apparatus and procedures

The experiments were conducted in the Pulsed Jet Facility (figure 2) of the Fluid Mechanics Research Laboratory located at the Florida State University. The air supply for the facility is provided from high-pressure (15 MPa) storage tanks connected to a high displacement air compressor. The tanks have a total capacity of $10\,m^3$ and could drive a jet with mass flow rate of $0.25\,kg\,s^{-1}$ continuously up to 40 min. The stagnation pressure and temperature in the settling chamber were maintained steady by two pneumatic valves and an inline electrical heater (192 kW) with automatic controllers. The pressure and temperature were kept at their nominal set value within a variation of ± 2 kPa and ± 0.5 K, respectively. The proper heating of the flow allowed matching the dimensionless parameters of Mach number, Reynolds number and Strouhal number of the simulated jet.

The settling chamber (length = 610 mm, internal diameter = 482.6 mm) assembly contained a rotating disk that is connected to a motor in a manner shown in figure 2. The rotational speed of the disk is controlled by a DC motor (Baldor SmartMotor, model CSM3615T-2). In order to minimize the air leak between the rotating disk and the end cap of the stagnation chamber, a teflon seal with the same geometric configuration as the disk is attached to the rotating disk. The rotating

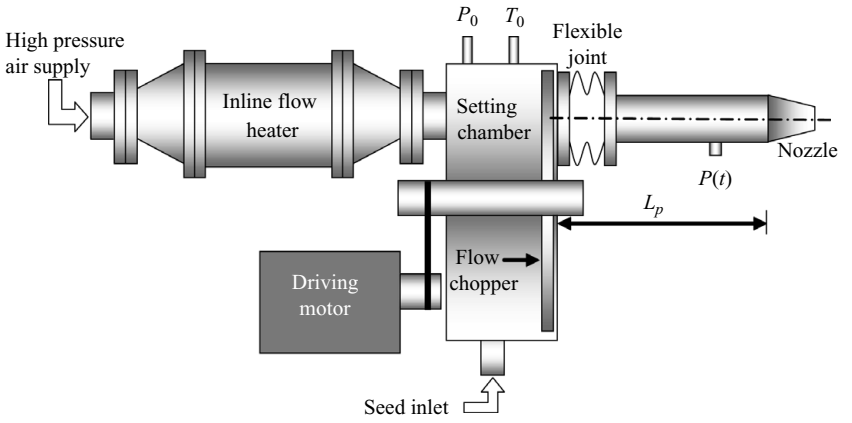

FIGURE 2. Schematic of the facility.

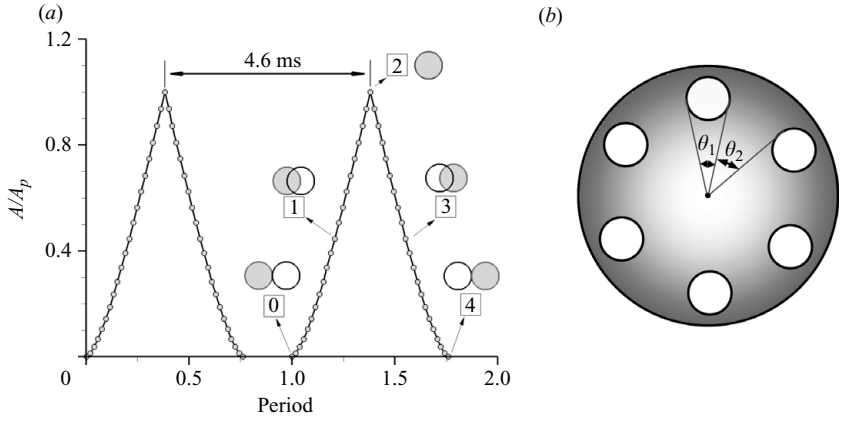

FIGURE 3. (*a*) The effective chopper opening area change in a period; Shaded circles: rotating disk opening; open circles: nozzle inlet opening (*b*) flow chopper geometry used to define the duty cycle.

disk ($D = 475$ mm) has six equally spaced circular holes with a nominal diameter $D_p = 76$ mm. The distance between the centres of the disk and the hole is 190.5 mm. The frequency of the pulses could be varied precisely up to 250 ± 1 Hz by changing the rotational speed of the motor. The end cap of the settling chamber has a circular opening of 76 mm in diameter. A 100 mm long flexible stainless steel joint (bellow, spring constant $= 30$ kN m^{-1}) connects the opening of the end cap to a straight smooth pipe of length $L_p = 228$ mm. The other end of the pipe is connected to the nozzle inlet. The calculated opening area at the entrance of the nozzle inlet as a function of period is given in figure 3(*a*). The shaded circles represent the rotating disk opening and the open circles represent the nozzle inlet opening. This configuration gives a duty cycle of 50 %. In the present configuration, the duty cycle is defined as the ratio of the angle subtended at the centre of the chopper by each hole to the total angle between two similar points of consecutive holes ($\alpha = \theta_1/(\theta_1 + \theta_2)$). The flow chopper has six holes spaced equally 60° apart and each hole subtends an angle of about 30° at the centre of the chopper giving rise to a duty cycle of 50 % (figure 3*b*).

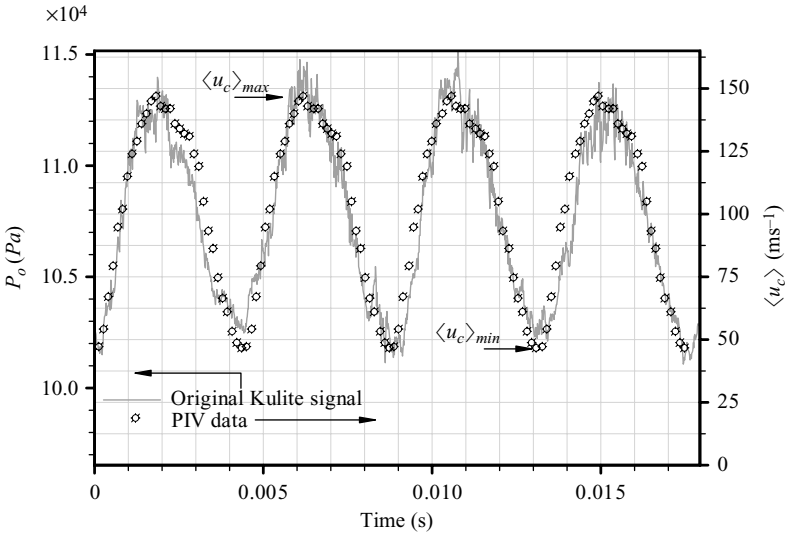

FIGURE 4. Total pressure and phase-averaged axial velocity variation with time at centre of nozzle exit, $St = 0.11$.

A 128 mm long nozzle has a smooth cubic spline contraction section with an area ratio of 2.24 ($D_{in} = 76$ mm; $D_{out} = 50.8$ mm) followed by a 25.4 mm straight section and the nozzle exit diameter d is 50.8 mm.

The stagnation pressure and temperature inside the settling chamber are measured using Omega pressure transducer (model PX215-100 AI) and an Omega K-type thermocouple, respectively. Since the stagnation pressure varies with frequency of operation, a second Omega pressure transducer is installed in the straight pipe preceding the nozzle. The static pressure in the straight pipe is calibrated against the nozzle exit centreline Pitot pressure measured using a RUSKA pressure transducer. The stagnation pressure is measured at the centre of the nozzle exit plane using a Pitot probe connected to a RUSKA pressure transducer. Simultaneous static pressure measurements from the static port located upstream of the nozzle are also recorded. Hence, for each stagnation pressure reading at the nozzle exit, there is a corresponding static pressure reading from the static pressure port ahead of the nozzle. From the calibration measurements, it is found that, for a given Mach number of the jet, the static pressure inside the straight pipe is not affected by varying frequency of operation. Hence, the static pressure in the pipe upstream of the nozzle exit is used to monitor the jet exit conditions accurately.

Typical unsteady total pressure time signal measured using a Kulite transducer (model no. XCE 062-100A) incorporated into a total pressure probe at the centre of the nozzle exit is shown in figure 4. The total pressure probe has a diameter of 2 mm. Since the diameter of the nozzle is 50.8 mm, the ratio of these diameters is about 1:25. Hence, the blockage effect due to the Pitot tube is small. The variation of the nozzle exit flow is depicted by the pressure-time signal in the figure. Also included in the figure is the phase-averaged axial velocity obtained using PIV (§ 2.1 and § 2.2). There appears to be a phase lag of about 7.8° (or 0.7 rad) between the pressure and velocity signals. The corresponding normalized p'_{rms} variation with the pulsing frequency is shown in figure 5. Here, P_0 is the total pressure at the centre of the nozzle exit plane and P_a is the ambient pressure. The variation of the normalized value of p'_{rms} is due

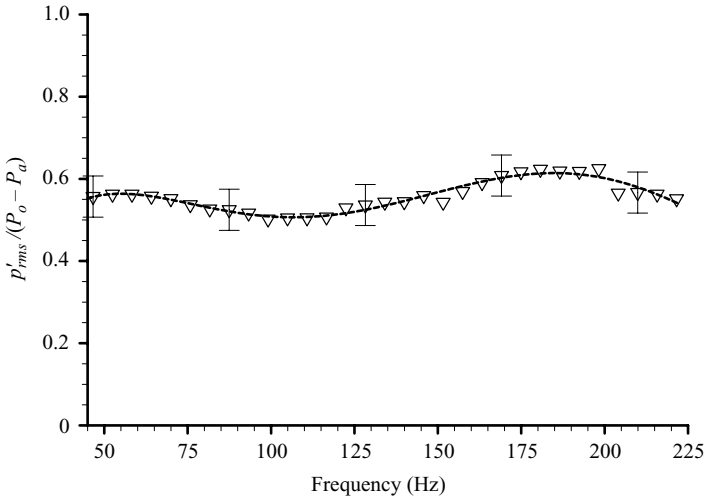

FIGURE 5. Normalized p'_{rms} variation with pulsing frequency at the centre of nozzle exit.

to experimental uncertainty which was measured to be about 5 %. The normalized magnitude of p'_{rms} assumes values within a range of 0.58 ± 0.04.

2.1. *Particle image velocimetry*

For PIV measurements, a dual cavity digitally sequenced Nd:YAG laser (Spectra Physics PIV400) was used. A light sheet of approximately 1 mm thickness was created by suitable combination of spherical and cylindrical lenses. The images were recorded simultaneously by two identical cross-correlation CCD cameras (sharpVISION 1400-DE) fitted with 55 mm ($f/2.8$) Nikon lenses. The resolution of the camera was $1.3\,\mathrm{k} \times 1\,\mathrm{k}$, which was operated in double exposure mode. In this mode of operation, with proper synchronization with 15 Hz laser trigger, the camera can acquire at a rate of 5 image pairs per second. In the present experiments, the jet was seeded with sub-micron ($\sim$0.3 μm) oil droplets generated by a modified Wright nebulizer, which supplied the particles to the main jet. Fog fluid (a solution of glycol and water) is used to generate the ambient seeding. The seed particles are supplied into the stagnation chamber, which then mix with the incoming air supply. The resulting jet from the nozzle is found to be uniformly distributed with the seed particles. The ambient air seeding is generated by a ROSCO 1600 fog generator. Alkislar (2001) estimated that more than 95 % of the particles generated by the present seeder would have a diameter of less than 0.5 μm, and the nominal particle diameter size would be no greater than 0.3 μm. In steady flows, using the nominal particle diameter of 0.3 μm, it was found that they track the flow quite accurately up to about $440\,\mathrm{m\,s^{-1}}$ (Alkislar, Krothaplli & Lourenco 2003).

The measurements were confined to the central plane covering $11d$ in the axial direction. A novel processing algorithm developed by Lourenco & Krothapalli (2000) was used to obtain accurate velocity data from the particle images with high spatial resolution. In this algorithm, the image is subdivided into interrogation regions and the average displacement of the 'ensemble' of particles in the interrogation area is measured using statistical correlation techniques. Thereafter, the interrogation area is further subdivided in order to identify individual particles using a particle detection scheme. In this scheme, a 'mask' is applied to eliminate the effect of particle

image truncation at the edges of the interrogation region and to eliminate spurious background due to reflections and parasite illumination. The particle detection scheme also generates a list of the centre of mass, position and form factor of each particle image. Once the particles are identified, a particle pairing procedure is applied based on the group displacement. The displacement is measured based on the maximum correlation between images of corresponding particles. Sub-pixel resolution is obtained by means of Gaussian interpolation. The measured displacement is assigned at the midpoint of the centre of masses of the corresponding particle images to generate the displacement position, which corresponds to a second-order evaluation of each displacement. The error in each displacement measurement is minimized by using a least-squares fitting algorithm. Second-order accuracy is maintained by assuming that the displacement field is well represented locally by a second-order polynomial

$$\boldsymbol{u} = \boldsymbol{a}x^2 + \boldsymbol{b}x + \boldsymbol{c}y^2 + \boldsymbol{d}y + \boldsymbol{e}xy + \boldsymbol{f}.$$

Since there are six unknowns in the equation, it requires at least six independent displacement position vectors. The algorithm ensures that there are at least ten values in the displacement positions list by dynamically adapting the sizes of the interrogation regions during the computation. The salient feature of this approach is that the flow field at any point is described with second-order accuracy including the derivates that are found by differentiating the above-mentioned equation. The main purpose of the least-squares method is to account for the velocity and seeding density gradients in addition to minimizing the local measurement error in comparison to that associated with individual particle image pairs. Even though an unstructured grid is used for obtaining the velocity vectors, the velocity field in the present study is presented at regular interval for ease of presentation.

The time evolution of the jet was captured by means of phase-locked measurements. A schematic of the instrumentation for the phase-locked PIV measurements is shown in figure 6. An incremental optical encoder attached to the rotating shaft was used to generate the necessary trigger signal for the image acquisition and processing programme (IDT ProVISION). The encoder had 720 increments in order to precisely mark the phase of the pulses. The pulse trigger train was synchronized with the fully closed pipe inlet just about to open (corresponds to the time at position '0' shown in figure 3*a*). This signal was divided such that it corresponded to the frequency of the laser and the camera. Finally, a delay on the divided signal was applied to generate the necessary phase trigger for the synchronized camera and laser strobe. All time delays were realized with an accuracy of about 1 ns. The laser frequency of 15 Hz requires the pulsation frequency to be a multiple of 15. The full cycle of a pulse was sampled in 60 phases with equal intervals. At every phase, 100 realizations were obtained. Phase-averaged velocity fields were computed by taking the mean of these instantaneous fields. The measurement uncertainty is estimated to be about 1 % and 10 % in phased-averaged velocity and random turbulence measurements, respectively, with a 95 % confidence level. The global mean quantities were calculated from phase-averaged values. A triple decomposition of the velocity data was carried out using a method similar to that of Alkislar *et al.* (2003).

Since the flow considered here is dominated by periodic oscillations, it is essential to ensure that the particles respond faithfully to flow oscillations. In our experiments here, due to highly unsteady nature of the flow, the particles experience higher accelerations. Mie (1996) has examined the effects of unsteady dynamic forces on spherical solid particles to estimate the cut-off frequency or cut-off particle size. For the conditions considered in our experiments, the maximum acceleration experienced

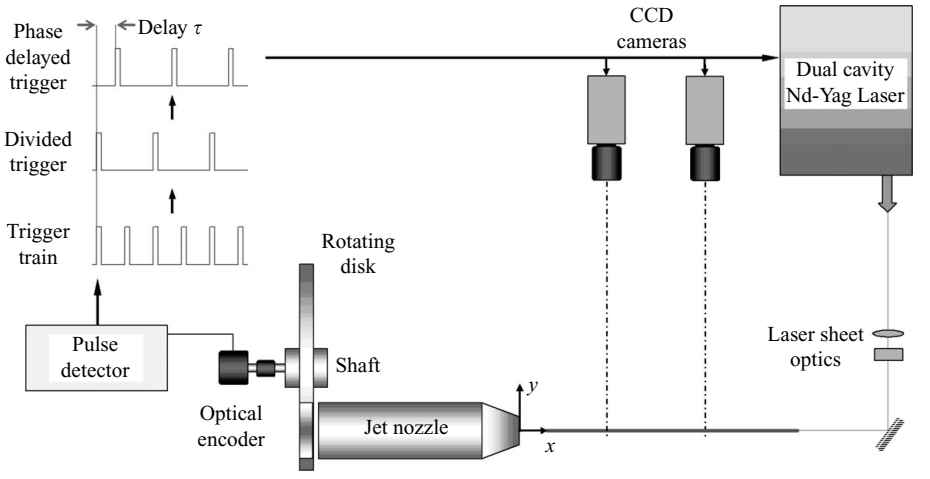

FIGURE 6. Schematic of PIV set-up.

by the particles is estimated to be about $211 \times 10^3\,\mathrm{m\,s^{-2}}$. For the maximum velocity observed in our experiments ($\sim 160\,\mathrm{m\,s^{-1}}$), the error in the velocity magnitude due to particle slip is estimated to be about 0.04 %. The analysis further shows that within the pulsing frequency range of 30–250 Hz, the particle size is sufficiently small enough that it responds closely to fluid velocity (Choutapalli 2006).

2.2. *Phase-locking technique*

The spatio-temporal evolution of the jet was obtained using the phase-averaging technique. Since an important portion of the flow field is periodic in time, the fluctuation away from a global mean $\bar{q}$ consists of a contribution from the periodic large-scale motion $\tilde{q}$ and a contribution q'' from the random fluctuations. When an ensemble of data is considered at a fixed phase, the mean of this ensemble describes the periodic motion $\tilde{q}$, with the vortices stationary at an average location. Fluctuations from the mean value at a fixed phase come from two main sources. In the following discussion, every fluctuation from the mean at constant phase will be considered as random q''. The fluctuations due to the variations in shape and location of the vortices in every sample (due to phase jitter) also contribute to this quantity; however, it is difficult to quantify the amount of the contribution.

Following the work of Reynolds & Hussain (1972), Bremhorst & Harch (1979) and Cantwell & Coles (1983), any flow variable, $q(x, t)$, can be decomposed into two components as shown in (2.1):

$$q(x,t) = \langle q(x,\tau)\rangle + q''(x,t), \tag{2.1}$$

where $< >$ is the average at a constant phase (which is also commonly used as the phase average), q'' is the random component and τ is the phase delay within the period of one pulse cycle. Then, the average at a constant phase is given by the following expression:

$$\langle q(x,\tau)\rangle = \bar{q}(x) + \tilde{q}(x,\tau), \tag{2.2}$$

where $\bar{q}(x)$ is the global mean and $\tilde{q}(x,\tau)$ is the periodic mean component.

In the present experiments, the average at a constant phase was obtained using the following equation:

$$\langle q(x,\tau)\rangle_m = \frac{1}{N_m}\sum_{i=1}^{N_m} q(x, t_i+\tau_m), \tag{2.3}$$

where N_m is the number of samples acquired at phase τ_m from the reference time t_i. The reference time is obtained from the optical encoder attached to the rotating shaft as shown in figure 2. One hundred samples at each phase were shown sufficient to achieve statistical convergence of the velocity field. A maximum mean value error of 5 % of the maximum velocity with 90 % confidence level was considered as a converged velocity field at a constant phase. The global mean is obtained using the following expression:

$$\overline{q}(x) = \frac{1}{M}\sum_{m=1}^{M}\langle q(x,\tau)\rangle_m . \tag{2.4}$$

The global mean values were found from the mean of the phase-averaged quantities as shown in (2.4) where M is the number of phases. In this study, $M = 30$ and 60 were used; therefore, the pulse cycle was sampled at 12° or 6° intervals based on the flow conditions. The phase-averaged velocity field was obtained using 100 samples, while the global mean velocity field was obtained using 3000–6000 samples. Once the global mean is calculated, the fluctuating component can be obtained from (2.2). The second-order correlations are calculated using the following equations:

$$\langle q''r''\rangle_m = \langle qr\rangle_m - \langle q\rangle_m\langle r\rangle_m, \tag{2.5}$$

$$\overline{\tilde{q}\tilde{r}} = \overline{\langle q\rangle\langle r\rangle} - \overline{q}\,\overline{r}, \tag{2.6}$$

$$\overline{qr} = \overline{q}\,\overline{r} + \overline{\tilde{q}\tilde{r}} + \overline{q''r''}, \tag{2.7}$$

and the total Reynolds stresses (conventional stresses obtained by classical Reynolds averaging) are simply the addition of the global fluctuating and global random components as

$$\overline{q'r'} = \overline{\tilde{q}\tilde{r}} + \overline{\langle q''r''\rangle} = \frac{1}{M}\sum_{m=1}^{M}(\tilde{q}\tilde{r} + \langle q''r''\rangle)_m. \tag{2.8}$$

To minimize the contribution due to phase jitter, in every phase, each of the 100 instantaneous velocity fields is correlated with the phase-averaged velocity field to obtain the correlation coefficients R_{uu}, R_{vv}. All the instantaneous flow fields which have a correlation coefficient greater than 0.8 are selected for further processing. The result based on this method of processing is shown in figure 7 for a given phase for $St = 0.06$. The figure shows the centreline velocity variation at a given phase. The velocity variation before the procedure is applied is shown by the solid line and the variation after it is applied is shown by the dotted line. It is seen that the maximum variation between the two cases due to jitter is about 2.8 % around $x/d = 5$. These velocity fields selected after the procedure is applied are considered to be good data samples for further analysis. Reynolds stresses here are associated with both the vortex location variations and the random fluctuations in velocity. These spatially resolved stresses at different phases are used in the following discussion.

In all the experiments, the data are acquired using two cameras with an overlap of a region covering the flow field of about 0.80 diameters. A weighted-average method is used to combine the data in the overlapping region. At the beginning of the overlap

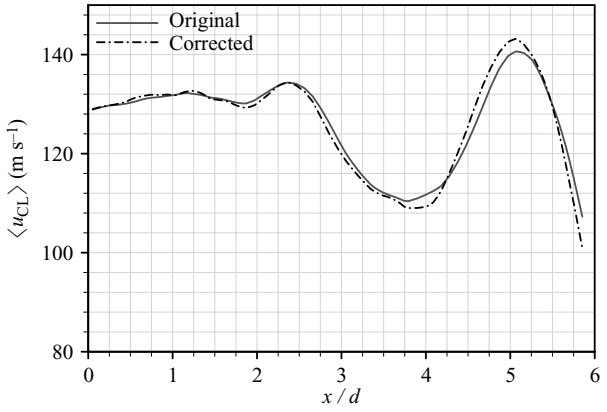

FIGURE 7. Phase-averaged axial velocity variation with and without correction for jitter; $St = 0.06$.

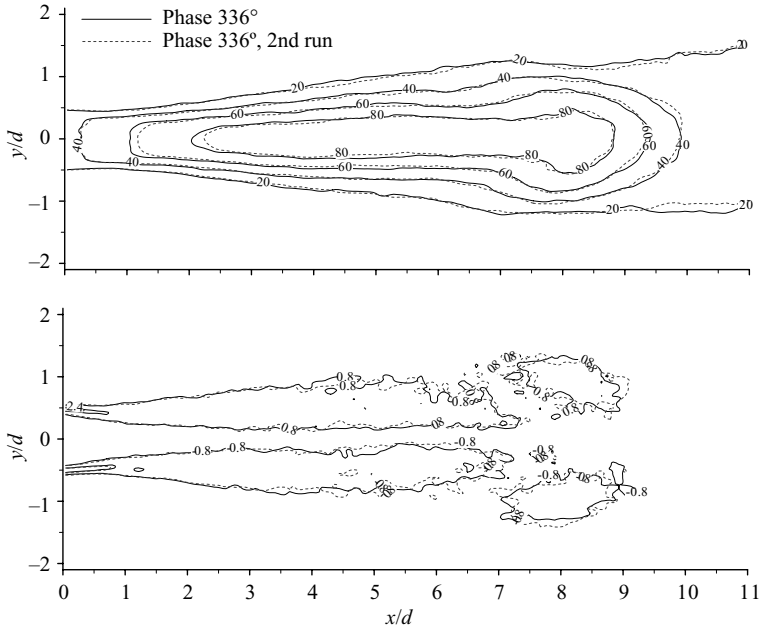

FIGURE 8. Comparison of (*a*) phase-averaged axial velocity contours, (*b*) normalized phase-averaged vorticity contours; $St = 0.06$.

region, the first zone is assigned a weight of one and the second zone is assigned a weight of zero. While moving towards the end of the overlap region, the weight of the first zone decreases linearly to zero whereas the weight of the second zone is increased linearly to one. The advantage of this technique is that it minimizes the mismatch of data at the edges of the combining zones (Alkislar 2001).

To validate this idea, PIV data from two different runs are compared in figure 8. The data of phase-averaged velocity and vorticity contour lines taken during two separate runs are compared at a phase angle of 336°. Since the data are obtained simultaneously from two cameras, it is imperative that they be accurately combined to show the complete flow field in the axial direction. It is seen from the figure that

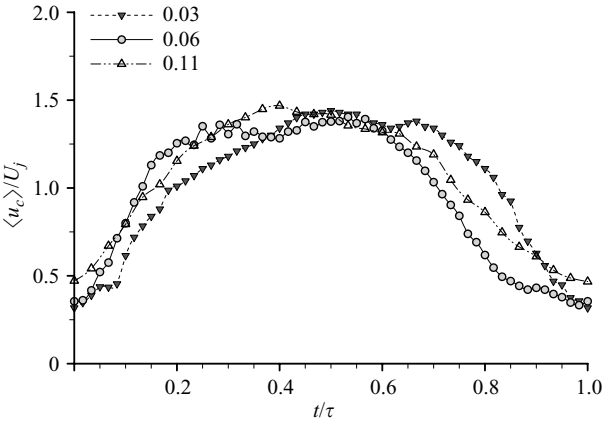

FIGURE 9. Phase-averaged exit velocity variation with time for different Strouhal numbers.

between $x/d = 5$ and 6, where the overlap of the two images occurs, there is a smooth transition of the contour lines for both the mean velocity and vorticy. For example, the normalized vorticity contours representing a level of 0.8 s^{-1} (figure 8*b*) for the two cases overlap reasonably well.

The uncertainty in the velocity measurements due to error in the particle displacement evaluation can be conservatively estimated to be 0.025 pixels (Lourenco & Krothapalli 2000). The accuracy of the mean and turbulent velocity field also depends on the number of samples acquired. In the present experiments, a typical acquisition consists of 100 vector fields for the phase-averaged flow field. Since the full cycle of the pulse is sampled over 30 to 60 phases with equal intervals, the global mean has 3000–6000 vector fields. This results in an uncertainty of about 1 % and 10 % in phased-averaged velocity and random turbulence measurements, respectively. In all the experiments, the time delay was chosen to give displacement not less than 5 pixels resulting in an error of 0.6 %. To further validate PIV measurements, a standard single hot wire set-up (DISA Type 55M10) was used to measure mean and turbulence profiles at selected downstream locations of a steady jet operating at an exit velocity of 105 m s^{-1}. We found very good agreement between the two sets of data (Choutapalli 2006). The velocity data derived from the unsteady pressure measurement, obtained using a Kulite probe (figure 4), were found to agree well with the PIV data (Alkislar *et al.* 2005): a further evidence of the success of the measurement technique. In these comparisons, the deviation of the Kulite probe measurements from PIV measurements is less than 2.0 %.

2.3. *Jet initial conditions*

The initial pulse characteristics play an important role in determining the jet structure. The velocity variation with time at the centre of the nozzle exit is used to characterize the pulse shape as shown in figure 9. Included in the figure are the data for the three different Strouhal numbers. The instant of time when the nozzle exit velocity reaches a minimum value at the centre is denoted as $t = 0$ for all the discussion. The spacing between the data points reflects the phase interval where the data were taken.

The measured values of important parameters that are characteristic of the initial pulse are given in table 1. Because of the manner in which the facility is built, it was difficult to achieve higher Strouhal numbers while maintaining a reasonable high mean velocity. The total pressure at the nozzle exit P_0 was maintained constant in all the experiments. However, the variation in the mean exit velocities shown

$St(=fd/U_j)$	P_0/P_a	U_j (m s^{-1})	$\frac{\tilde{u}_{c,rms}}{U_j}$	$\frac{\langle u_c\rangle_{max}-\langle u_c\rangle_{min}}{U_j}$	$\frac{\langle u_c\rangle_{max}}{U_j}$	L/d	$\frac{M_{exit}}{M_{mass\ avg}}$	$\frac{E_{exit}}{E_{mass\ avg}}$
0.03	1.1	88.1	0.41	1.12	1.44	29.4	1.08	1.29
0.06	1.1	92.3	0.42	1.02	1.40	16.7	1.11	1.36
0.11	1.1	100.5	0.42	1.00	1.47	9.4	1.15	1.40

TABLE 1. Operating conditions and parameters.

in table 1 is due to the variation in the nozzle exit static pressure at different pulsing frequencies. For the three Strouhal numbers considered in the paper, the resulting fluctuation magnitudes and the maximum velocity within a period remain relatively constant. The slug length to nozzle diameter (L/D) ratio ($L=t\overline{U}_e/d$ (where $\overline{U}_e=4/(\pi d^2\tau)\int\int_0^\tau u\mathrm{d}t\,\mathrm{d}A$ at the nozzle exit plane) varies from 9.4 to 29.4. Since these values are much greater than the characteristic stroke ratio of 4.0 (ratio that differentiates between a single vortex ring and the vortex ring with a trailing jet) observed by Gharib, Rambod & Shariff (1998), it is expected that the dynamics of the pulsed jets in our study, which are close to realistic operating conditions of pulsejet engines, would be different from those available in the literature thus far.

The variation of time-averaged momentum flux $M_{exit}=(1/\tau)\int\int_0^\tau \rho u^2\mathrm{d}t\,\mathrm{d}A$ and energy flux $E_{exit}=(1/\tau)\int\int_0^\tau \rho u^3/2\,\mathrm{d}t\,\mathrm{d}A$ at the nozzle exit with St is given in table 1. In a steady jet, these ratios assume a value of unity. However, in an unsteady jet, the magnitudes of the two ratios depend on the nature of the temporal variation of the exit velocity. The energy flux represents the extra work necessary to be expended in producing a pulsed jet as compared to a steady jet with the same mass flow rate. In an unsteady jet, the momentum and energy will have contributions due to the overpressure in addition to the momentum and energy flux terms M_{exit} and E_{exit}, a discussion of which is deferred to § 3.

The global mean and phase-averaged mean velocity profiles at the nozzle exit are examined using the data at $x/d=0.1$. This downstream location is selected to avoid any contamination to the data due laser light reflections from the nozzle exit. The velocity profiles shown in figure 10 are representative of the background jet flow preceding the formation of the vortex. The top-hat velocity profiles with turbulent shear layer are observed as shown in figure 10. With increasing Strouhal numbers, the magnitude of phase-averaged axial velocity of the background jet increases as shown in figure 10(b). These observations indicate that the initial pulsed jet flow being studied here is a turbulent pulsed jet with sufficiently large pulsation magnitude that is representative of a realistic pulse jet engine exhaust (Choutapalli 2006). Furthermore, figure 11(a) shows the three-dimensional axial mean velocity for $St=0.06$ at the nozzle exit. The velocity profiles taken on two perpendicular diametric planes are shown in figure 11(b). It can be seen from the figure that the flow field at the nozzle exit is symmetric. In all the experiments, the Reynolds number of the jet, based on the nozzle mean centreline exit velocity and the exit diameter, is about 3.4×10^5. The stagnation temperature of the jet was kept constant at 313 K.

3. Results and discussion

3.1. *Overall structure of the pulsed jet*

The modulation of the exit velocity in time generally results in a series of vortex rings, produced once per cycle, riding over a background flow (figure 12). A vortex

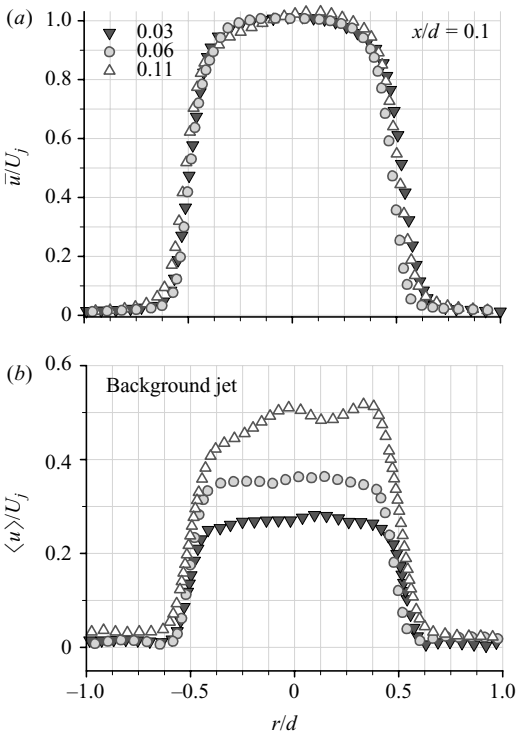

FIGURE 10. Nozzle exit ($x/d = 0.1$) conditions for the background jet: (a) global mean axial velocity profiles, (b) phase-averaged axial velocity profiles.

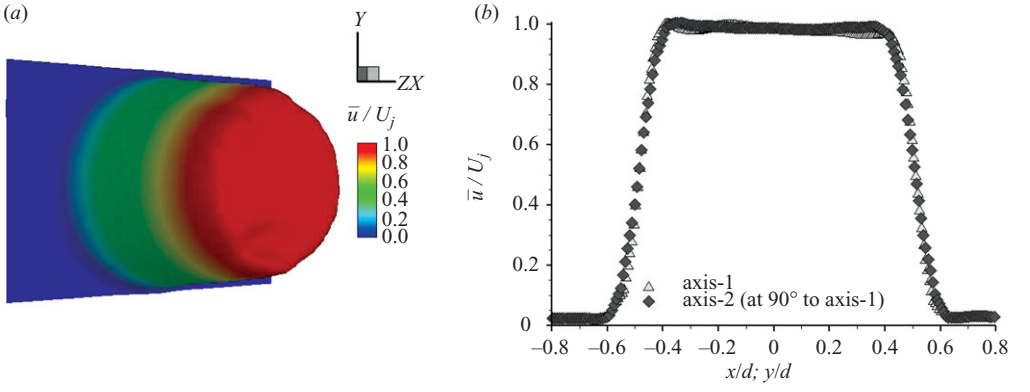

FIGURE 11. 3D PIV data at the nozzle exit plane ($x/d = 0.1$) for $St = 0.06$; (a) global mean axial velocity contours and (b) global mean axial velocity profiles along two perpendicular diametric planes.

ring begins to form at the instant the velocity at the exit begins to increase. As in the formation of a conventional vortex ring, the ring grows in size, its circulation increases, convects downstream and at some later time detaches from the trailing jet, commonly referred to as pinch-off (Gharib *et al.* 1998). In the present experiments, the convection velocity of the ring is approximately $0.6U_j$.

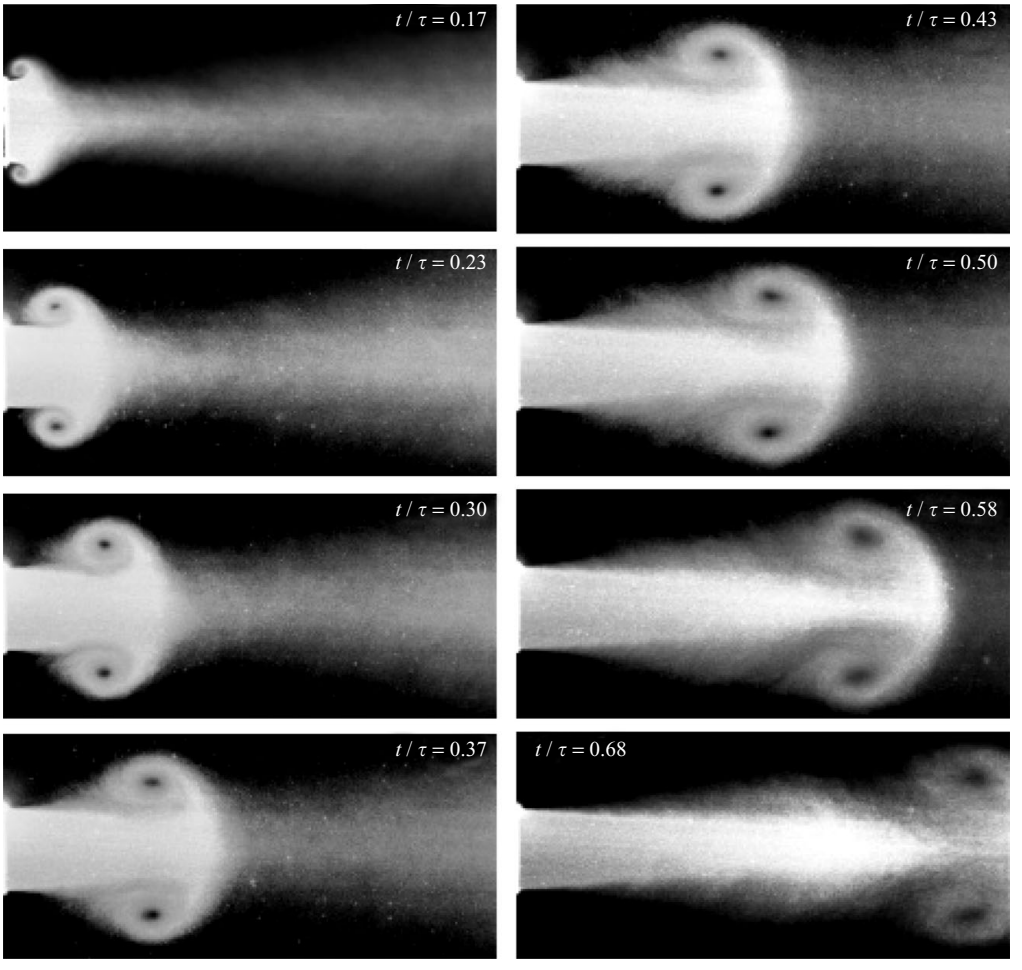

FIGURE 12. Phase-locked flow visualization images of a pulsed jet at $St = 0.06$.

There are some crucial differences between an isolated vortex ring and the ring in a pulsed jet. How the rings and the background jet evolve individually and through mutual interaction dictates the downstream evolution and the properties of a pulsed jet. In the present experiments, with the Reynolds number being high enough that the rings and jets are turbulent and the variation in $\langle u_c \rangle_{max} - \langle u_c \rangle_{min}/(U_j)$ being small for the different cases, the governing parameter is T^* or St.

Figure 13 shows contour plots of the phase-averaged axial velocity and azimuthal vorticity for different St numbers studied. At each St, five phases are included starting with $t/\tau = 0.2$. The axial velocity and vorticity contours are shown in the bottom and top half of each plot, respectively. Also shown in each plot is the variation of the axial centreline velocity $\langle u_c \rangle$. The exit velocity at each phase may be obtained from axial centreline velocity curve. These figures give the salient features in the near field ($x/d < 10$) of the pulsed jet as the St is varied.

We discuss the high $T^* = 29$, 16.7 (i.e. low $St = 0.03$, 0.06) cases first. Data at these conditions suggest that the rings are produced at a low frequency and are spaced apart. The initial spacing between adjacent vortices Δx_{ring} is approximately $0.6T^*d$. But for the presence of the background flow, the rings would be similar to individual

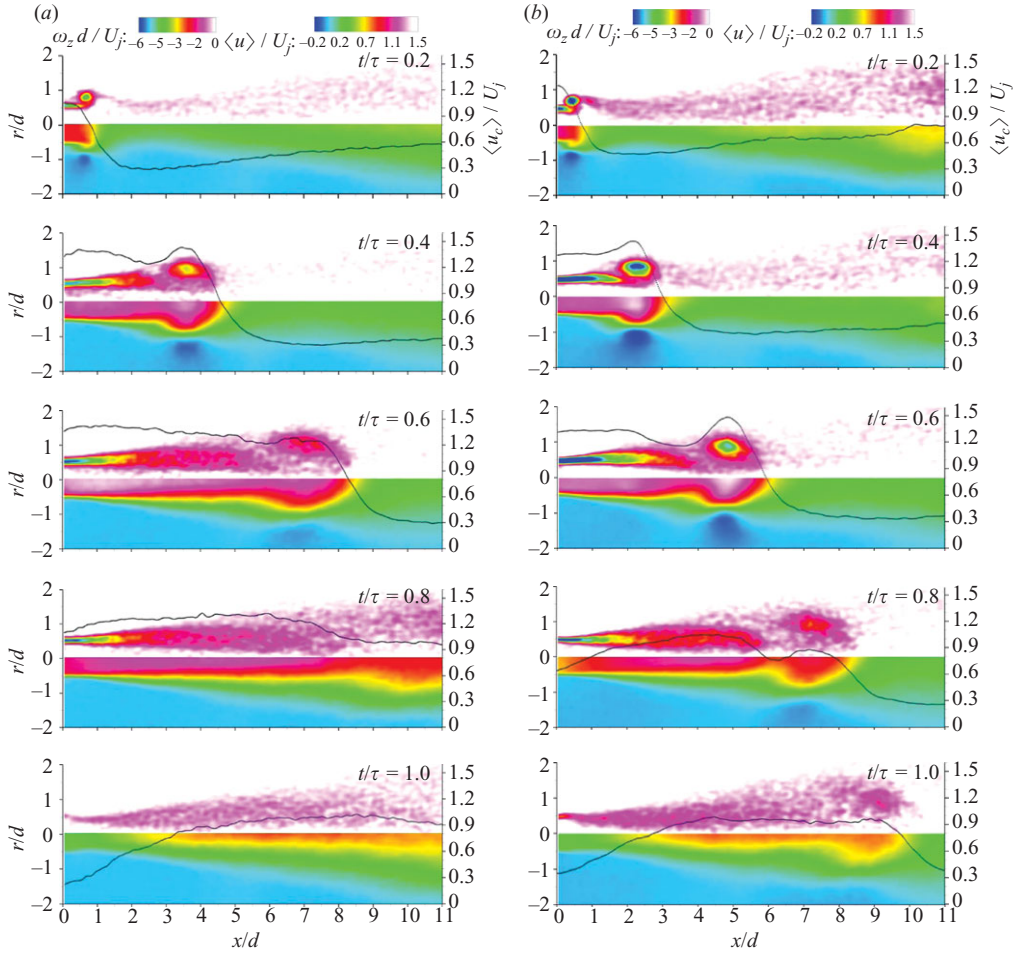

FIGURE 13. For legend see facing page.

vortex rings without interaction. Considering the $T^* = 29$ case, we observe that as the exit velocity begins to increase at time $t = 0$, the shear layer starts to roll up (see $t/\tau = 0.2$) and by $t/\tau = 0.4$, the vortex ring is completely formed and pinched at roughly $4d$ from the exit. There is substantial decay in the strength, as measured by the peak vorticity of the ring as it convects downstream; at $t/\tau = 0.8$, the ring is about $10d$ from the nozzle exit, and at $t/\tau = 1$ the ring has moved out of the camera range. Some of the vortex ring properties are discussed in § 3.2.

As mentioned above, this vortex ring is different in some respects from an isolated ring. The fluid that exits the tube and eventually forms the ring is seeing fluid upstream in the ambient having a finite axial velocity; for convenience, we term this fluid ahead of the ring as the background jet. Similarly, the fluid behind the ring, i.e. the trailing jet, has a finite velocity. The background jet has a velocity small compared to the axial velocity in the ring and corresponds to fluid coming out of the nozzle when the exit velocity is around the minimum in the cycle. On the other hand, the trailing jet axial velocity is similar in value, and sometimes higher than the axial velocity in the ring. Note that the ring is composed of fluid corresponding to phases when the exit velocity is increasing in time, and the trailing jet to that when the exit velocity

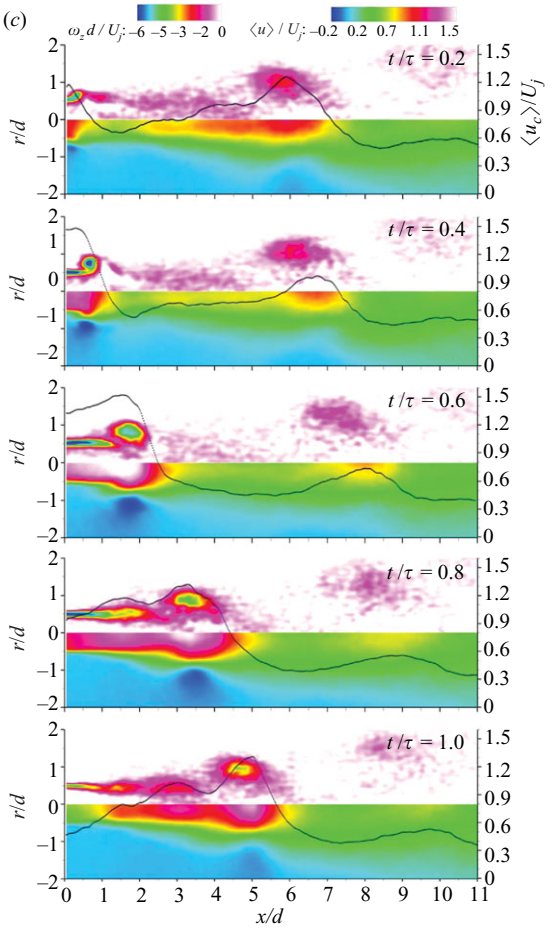

FIGURE 13. Evolution of a pulsed jet; (*a*) $St = 0.03$, (*b*) $St = 0.06$, Top: phase-averaged out-of-plane component of the vorticity; bottom: phase-averaged axial velocity. The solid line is the centreline velocity profile at each phase, (*c*) $St = 0.11$.

is around the maximum. In the above discussion, axial velocity refers to that on the centreline. These observations are made clear by examining the plots of the centreline velocity versus x/d in figure 13(*a*). The variation in front of the ring is typical of that found in an isolated ring (e.g. $t/\tau = 0.4$), except the velocity decays down to the background jet velocity value instead of to zero. For $t/\tau = 0.4$ and 0.6, the velocity magnitude in the trailing jet is about the same as that corresponding to the ring, but at $t/\tau = 0.8$ the trailing jet velocity is higher. The demarcation of the flow other than the ring into background jet and trailing jet is more a matter of definition and convenience. One can argue that the background jet is nothing but the end of the trailing jet of the preceding vortex ring.

The flow evolution for $T^* = 16.7$ ($St = 0.06$), as shown in figure 13(*b*), is similar to that for $T^* = 29$. Because of the reduced time period, the ring from the previous cycle just leaves the frame at $x/d = 10$ as the new one forms ($t/\tau = 0.2$). As the frequency increases the distance between adjacent rings reduces. For example, for $T^* = 9.4$ ($St = 0.11$) (figure 13*c*), the ring from the previous cycle is about $6d$ from the exit when the new one has begun to form. For this case, the rings are perhaps

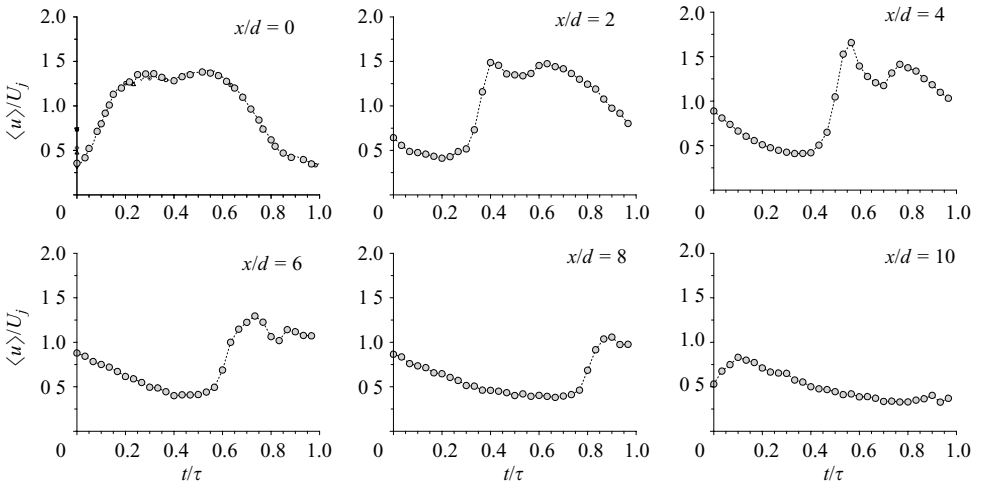

FIGURE 14. Temporal variation of the phase-averaged centreline axial velocity at different axial distances for $St = 0.06$.

close enough that the trailing jet of the leading ring influences the dynamics of the one following.

At the next higher frequency, $T^* = 9.4$ ($St = 0.11$) (figure 13*c*), two vortex rings are seen in the frame spaced $\Delta x_{ring} \approx 5d$. The spacing between the rings has decreased and the rings remain clearly distinguishable only till about $7d$ from the nozzle exit. At $t/\tau = 1.0$, a weaker secondary ring seems to form in the shear layer in addition to the primary one. The secondary ring is weaker and shorter lived. As discussed by Krueger & Gharib (2005), this could be due to the gradual pulse termination as shown in figure 4. It could also be caused by the shear layer becoming unstable at the 'preferred' mode of the jet (Crow & Champagne 1971) corresponding to the first harmonic of the forcing frequency.

In all the cases, a vortex ring begins to form when the exit velocity starts to increase in time. The strong spatial decline of axial velocity is just ahead of the ring with a maximum in u_c usually being coincident with the core. Another common feature associated with the ring, till it is strong enough, is the existence of negative u regions (shown in blue colour contours in the bottom half of the figure).

A feature of the initial evolution of a pulsed jet is brought out by plotting the variation in time of the axial centreline velocity at a fixed location. This is the velocity that would be recorded by, for example, a fixed hot-wire probe. Figure 14 shows such plots at $x/d = 0$, 2, 4, 6, 8 and 10 for the $St = 0.06$ jet. The variation in time of the exit velocity ($x/d = 0$) develops a sharp gradient as reflected in the profiles at $x/d = 2$ and $x/d = 4$. This steepening is associated with the ring formation and looks similar to that observed during shock formation in unsteady compressible flows. The similarity is limited to the fact that in both cases nonlinear processes lead to the steepening. In most of the experiments, incompressible vortex rings have been produced with an impulsive or near-impulsive motion of a piston (Shariff & Leonard 1992). In experiments where an open-ended shock tube is used to produce a ring (Arakeri *et al.* 2004), the exit velocity variation in time has an initial very sharp increase from zero as the shock exits the tube, followed by a slower increase as expansion waves enter the tube and the high-pressure fluid behind the shock accelerates.

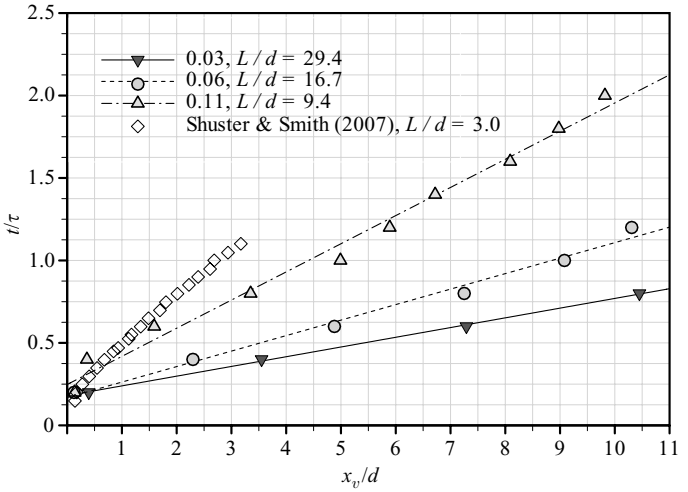

FIGURE 15. Temporal variation of the ring position in the axial direction for different St.

The peak in the velocity (e.g. at $t/\tau = 0.6$, $x/d = 4$) is associated with the presence of the ring. The velocity before this time corresponds to the background jet, and the high velocity after the ring corresponds to the trailing jet. When the ring is strong, there is a local minimum in the velocity demarcating the ring and trailing jet. Clearly, at a fixed time, a similar signature of velocity with x is seen (figure 13a–c), except that increasing time should be viewed as decreasing x.

The quantitative description of the spatio-temporal features of the pulsed jet described above is given in the following sections. This description includes evolution of the vortex ring, the background and trailing jets and their interactions. Given the high Reynolds numbers jet flows considered in these experiments, both the periodic and random components of the turbulent stresses play an important role in the flow evolution.

3.2. *Flow evolution*

Figure 15 shows the variation of the ring position with non-dimensional time for the different St; the ring position x_v at a particular time is derived from the phase-averaged vorticity plots of the type shown in figure 13. For each St, a straight line has been fitted through the data; inverse slope of the line gives the average convection velocity or celerity of the ring. Ring position data are available till $x/d = 11$, the extent to which PIV images were recorded. The data of Schuster & Smith (2007) are also shown for comparison in the figure. A higher frequency leads to more frequently produced and spatially closely spaced rings. Closer spacing of the rings also results in their earlier demise. When the data in figure 15 are plotted using a different non-dimensionalization for the time, there appears to be a collapse of the data for $St > 0.06$ as shown in figure 16. The data for 0.03 are slightly offset with the slope being the same as that of the other data. The linear variation indicates a vortex ring convection velocity $U_{ring} \approx 0.6U_j$, which is independent of the forcing frequency at least for the limited range considered here. There seems to be slight increase in ring convection velocity with decreasing L/D as suggested by the synthetic jet data of Schuster & Smith (2007) and the data of Choutapalli (2006) at $St = 0.24$ and 0.42.

The phase-averaged ring circulation variation with downstream distance is shown in figure 17. The maximum circulation for the $St = 0.03$ and 0.06 cases is about

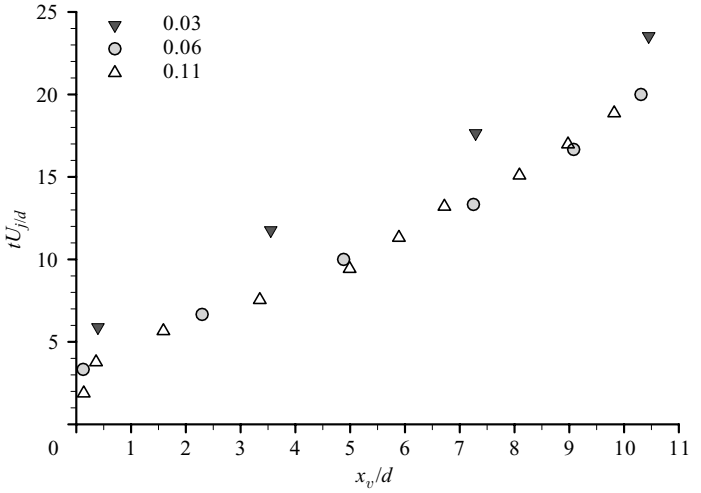

FIGURE 16. Vortex ring position variation in the axial direction with a non-dimensional time.

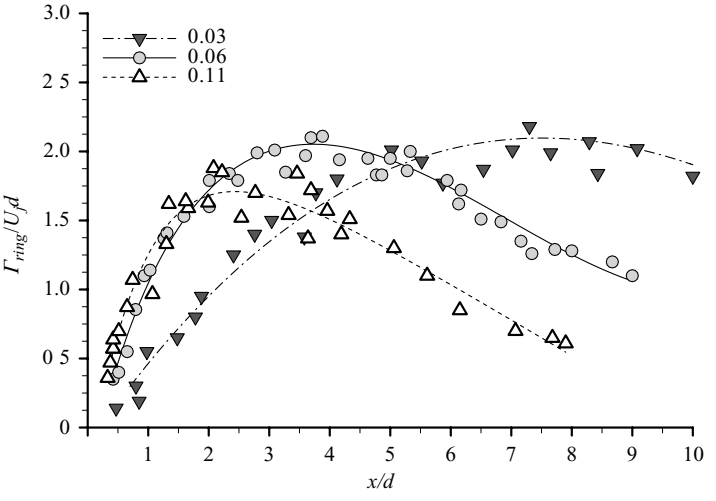

FIGURE 17. Variation of vortex ring circulation with downstream distance.

the same ($\sim 2U_j d$) and slightly less ($\sim 1.7U_j d$) for $St = 0.11$, though the distance at which the maximum is achieved decreases with increasing St. Similar values for the normalized ring circulation were also observed by Rosenfeld, Rambod & Gharib (1998) and Mohseni, Ran & Colonius (2001) for single pulses. In the three cases under consideration, we observe a build-up of circulation, and when the ring cannot accommodate any more vorticity it pinches off from the trailing jet. As shown in figure 18, the maxima in the peak vorticity for all the cases occur within $x/d = 2$, corresponding to the rolling up of the shear layer from the nozzle wall.

The decay with distance of the rings is accompanied by a reduction in the modulation of, for example, the phase-averaged centreline velocity as seen in figure 14. Figure 19 shows for the three Strouhal numbers the variations of the r.m.s. of the fluctuation in the periodic component of centreline axial velocity. The $\sqrt{\tilde{u}^2}/U_j$ can be considered to be a measure of the unsteadiness of the jet, and its

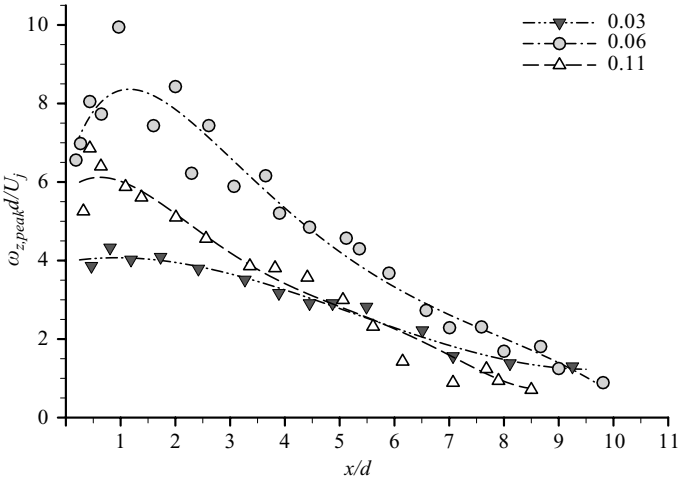

FIGURE 18. Vortex ring peak vorticity variation with downstream distance.

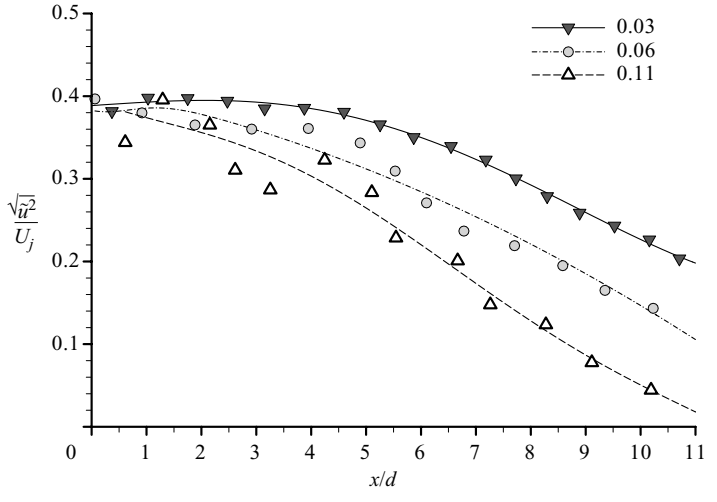

FIGURE 19. Axial velocity fluctuation of the periodic component variation along the jet centreline.

decay indicates the transition from a pulsed to a steady jet. The reduction in the peak vorticity seen in figure 18 is mostly due to turbulent diffusion. Since we are looking at phase averages, 'jitter' in the data may also be contributing to this reduction. When compared to the peak vorticity decay, the ring circulation decays rather slowly (figure 17). The decay in circulation is due to its loss to the trailing jet and, when the vortex core becomes large enough, through diffusion of vorticity in the flow field.

3.3. *Different regions of the jet*

At low enough frequencies, the rings are sufficiently spaced apart and we can usefully divide the flow into three components composed of the ring, trailing jet behind the ring and background jet ahead of the ring corresponding roughly to the region of low axial velocity. In the limited ($x/d < 11$) range of data we have, it is useful to investigate how these three components of the jet evolve. For the following discussion,

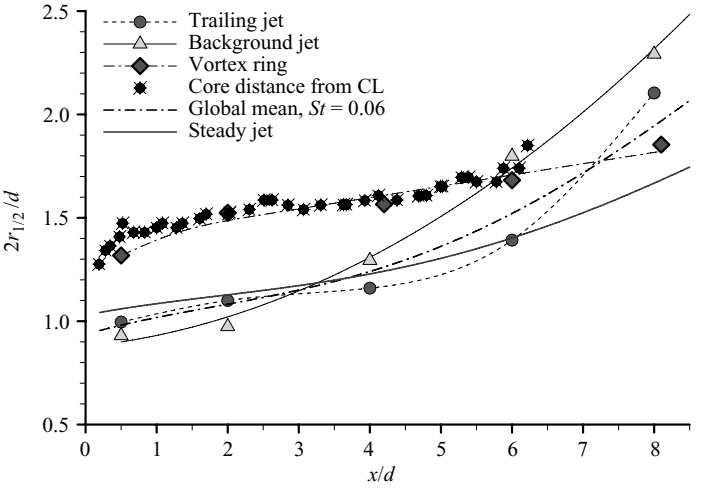

FIGURE 20. Downstream evolution of the half-width for the vortex ring, trailing and background jets; $St = 0.06$.

we consider the $St = 0.06$ jet in detail. We choose the location $3d$ behind the ring to represent the trailing jet, and the point of minimum axial centreline velocity at a given phase to represent the background jet.

Figure 20 shows the variations of the half-width with x/d for each of the three components of the jet. For comparison, the variation of the global mean half-width and that of the steady jet is included. The steady jet data referred to in this paper are also obtained from the present experimental set-up. The ring half-width, which happens to coincide with the vortex core distance from the centreline, shows a rapid increase for $x < 0.5d$, a region of vortex ring formation, and thereafter the increase is gradual. The half-widths corresponding to the trailing and background jets show initial slow growth, similar to that for a steady jet, and then increase relatively rapidly overtaking the ring half-width.

The centreline axial velocity variations for the three components of the pulsed jet, shown in figure 21, are quite different from each other. However, the global mean of the centreline velocity of the $St = 0.06$ jet and that of the steady jet shows similar variations. Till about $x/d = 4$, the centreline velocities corresponding to the ring and trailing jet are of similar magnitude. At about $x/d = 8$, the trailing jet velocity rapidly drops to nearly the background jet value, which, interestingly, is almost constant with distance.

The phase-averaged axial velocity profiles with r/d for different components of the jet at various downstream locations are shown in figure 22. In the initial few diameters, the profiles corresponding to the ring show the negative velocities in the outer parts of the ring; with increasing x/d in the central region, the profiles change from top hat to rounded. In the trailing jet, the profiles of axial velocity show some features that would be found in a steady jet: the initial region ($x/d \leqslant 4$) with distinct shear layers and profiles having a flat central portion, indicating a 'potential core', followed by Gaussian type profiles after merger of the shear layers. However, as seen in figure 21, the centreline velocity decays much more rapidly than in a steady jet. In contrast, for the background jet as noted above, the centreline velocity in fact slightly increases with x/d (figure 21). The background jet is taken to be the fluid ahead of the vortex ring and behind the trailing jet of the preceding pulse. The small

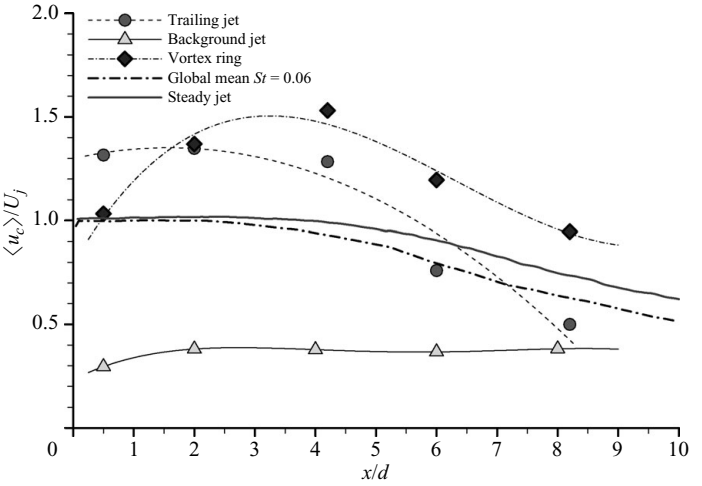

FIGURE 21. Phase-averaged centreline velocity for different components of the jet; $St = 0.06$.

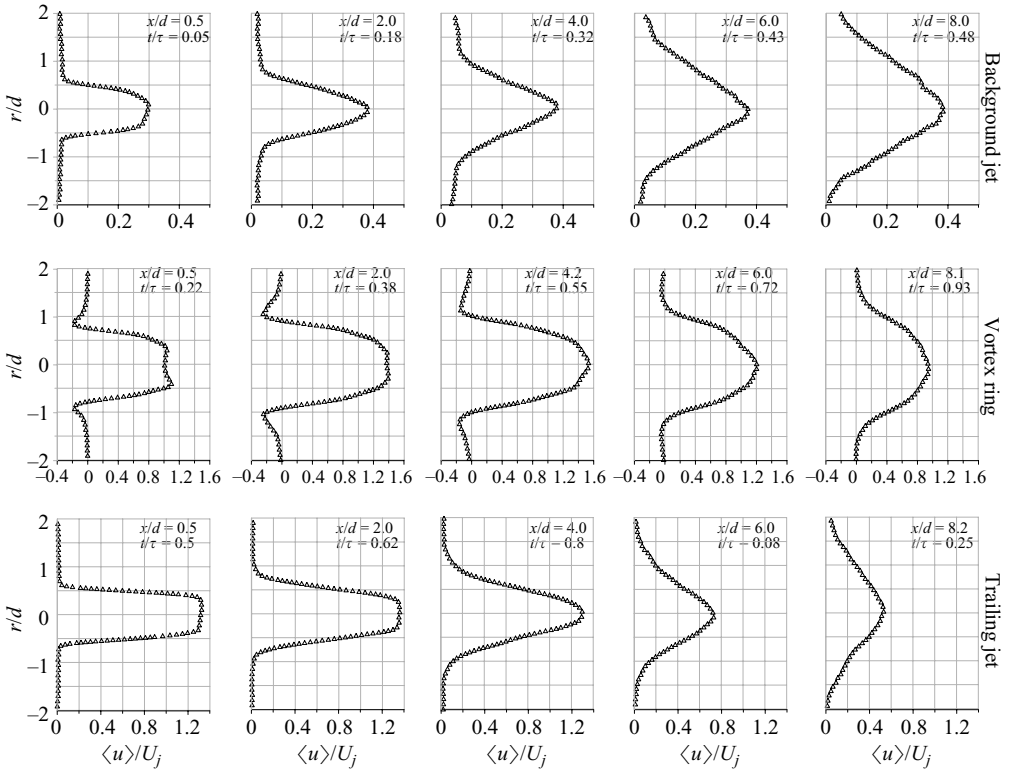

FIGURE 22. Phase-averaged axial velocity profiles at different downstream locations at $St = 0.06$; top: background jet; middle: vortex ring and bottom: trailing jet.

increase in velocity of the background jet in the figure is due to the slowing down of the trailing jet of the preceding pulse. As a result, the background jet region is 'contaminated' with the fluid of the new vortex ring and the preceding pulse's trailing jet. Hence, there is a slight increase in the velocity of the background jet. As seen in

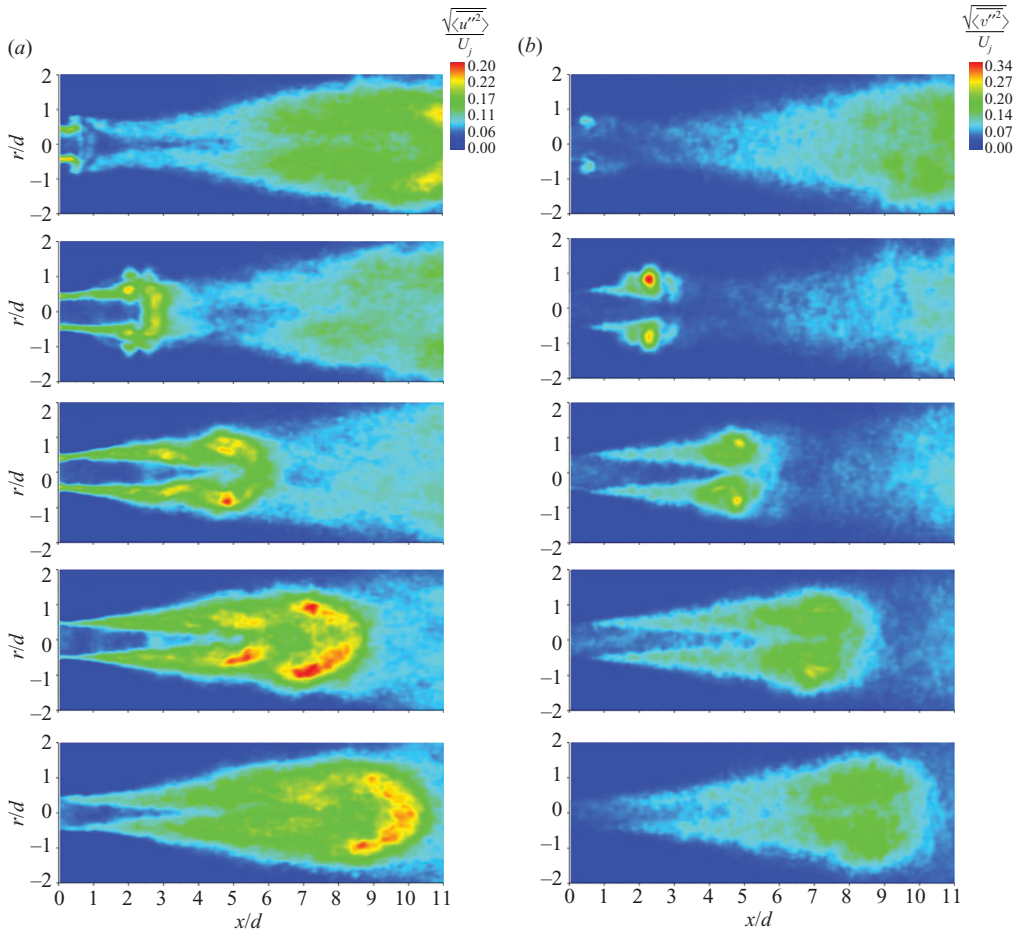

FIGURE 23. For legend see facing page.

the figure, the profiles even at small x/d do not have flat regions and look distinctly non-Gaussian for $x/d > 4$.

Figure 23 shows the contour plots for the $St = 0.06$ jet of the phase-averaged random turbulent velocity components $\sqrt{\langle u''^2\rangle}/U_j$, $\sqrt{\langle v''^2\rangle}/U_j$ and $\langle u''v''\rangle/U_j^2$. The peaks in the axial component $\sqrt{\langle u''^2\rangle}/U_j$ are near the nose and vortex cores of the ring and in the shear layers of the trailing jet. Maximum values of the radial random component $\sqrt{\langle v''^2\rangle}/U_j$ are found in the vortex cores and in the shear layers of the trailing jet (Glezer & Coles 1990). In the trailing jet region, the maximum Reynolds shear stress $\langle u''v''\rangle/U_j^2$ regions almost coincide with the maximum vorticity regions (compare figure 23*c* and figure 13*b*). For the vortex ring, till about $x = 4d$, regions of both positive and negative Reynolds shear stress can be seen at the ring core. As the ring develops, maximum shear stress occurs around the core on the outside regions of the ring. The contour plots of the periodic stress components $\tilde{u}\tilde{u}/U_j^2$, $\tilde{v}\tilde{v}/U_j^2$ and $\tilde{u}\tilde{v}/U_j^2$, not included here, show large values as compared to those of the random components (Choutapalli 2006).

Profiles of the phase-averaged axial (figure 24*a*) and radial (figure 24*b*) components and phase-averaged Reynolds shear stress (figure 24*c*) of the random fluctuations

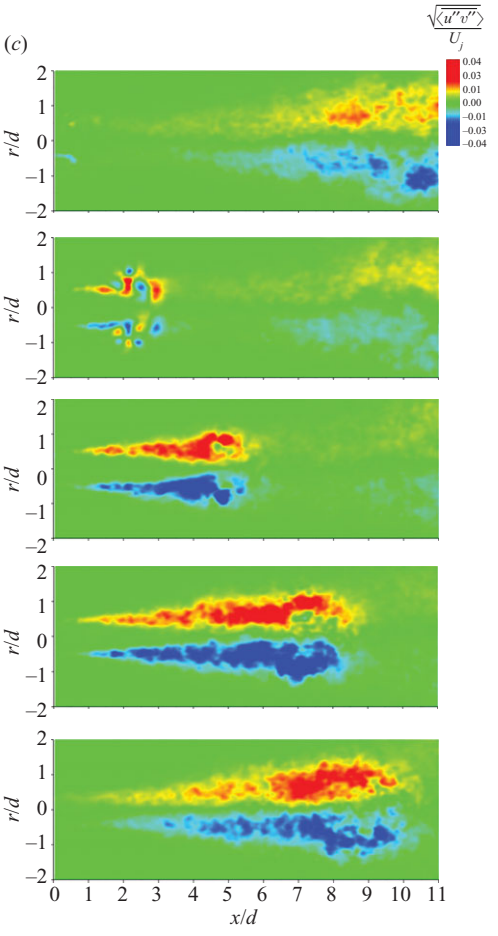

FIGURE 23. Contours of phase-averaged random turbulence components at different phases during a cycle for $St = 0.06$; (*a*) axial component, (*b*) radial component, (*c*) Reynolds shear stress of random fluctuations.

at different x/d in the three regions of the pulsed jet reveal information that is not obvious in the contour plots. In the ring, once it is formed, profiles of both the axial and radial fluctuations show maxima near the cores. The levels of the two turbulent fluctuations and the Reynolds shear stress are highest in the ring at all x/d. For all the three quantities and for $x/d < 5$, double peaks associated with the shear layers are seen in the trailing jet and to a lesser extent in the background jet. The shear stresses in the background jet are particularly small (figure 24*c*) as compared to the corresponding turbulent fluctuations of the vortex ring and the trailing jet (figures 24*a* and 24*b*). In spite of fluctuation levels being different in trailing and background jets, it is observed that the correlation coefficient $\overline{u''v''}/\sqrt{\overline{u''^2}}\sqrt{\overline{v''^2}}$ assumes a value between 0.5 and 0.6 for both, a value close to that in a steady jet.

Production of the random component of the turbulent kinetic energy is given by $\langle u''u''\rangle\frac{\partial\langle u\rangle}{\partial x} + \langle u''v''\rangle(\frac{\partial\langle u\rangle}{\partial r} + \frac{\partial\langle v\rangle}{\partial x}) + \langle v''v''\rangle\frac{\partial\langle v\rangle}{\partial r}$, which has three components: The second term is the familiar work done by the Reynolds shear stress on the mean (phase-averaged) velocity gradient, which is the dominant term in shear layers. The other two terms, which are not important in thin shear flows such as boundary layers and

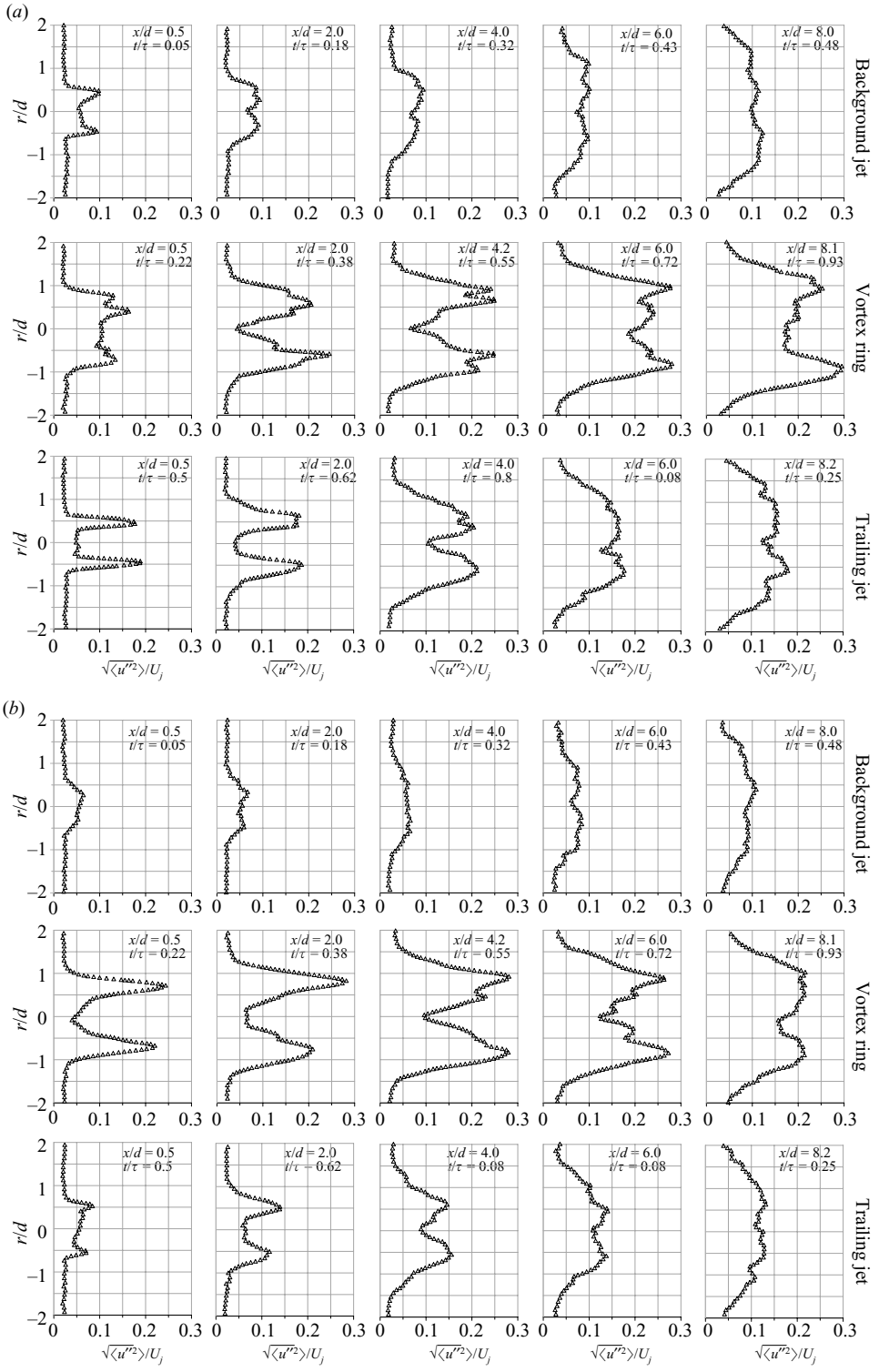

FIGURE 24. For legend see facing page.

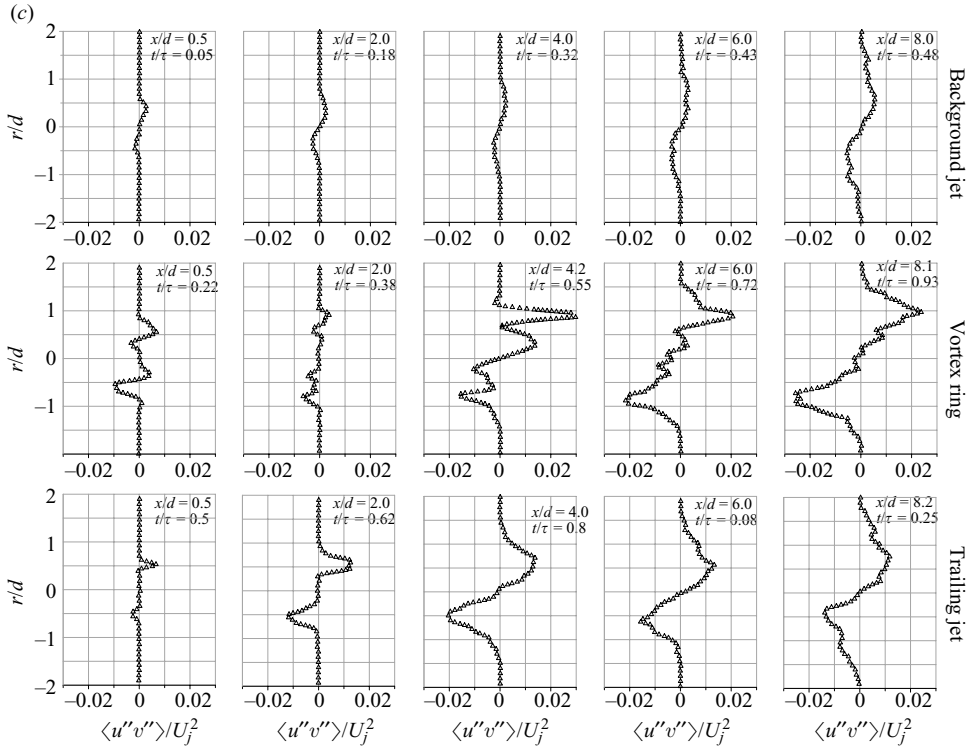

FIGURE 24. Profiles of phase-averaged random turbulence quantities for the three components of the jet at different downstream locations for $St = 0.06$; (*a*) axial component, (*b*) radial component, (*c*) Reynolds shear stress of random fluctuations.

jets, are the products of the normal turbulent stresses and the corresponding normal velocity gradients. The uncertainty in the parameter (TKE/U_j^2) is $\pm 5 \times 10^{-5}$ in the present experiments.

Figure 25 shows contour plots of the total production at different phases within a cycle. These contour plots look remarkably similar to those of random turbulent fluctuations shown in figure 23; regions of high turbulence production and regions of large turbulent fluctuations nearly coincide. There are two regions of dominant turbulence production, one associated with the ring and the other with the trailing jet shear layers. High turbulence production near the nose of the ring is mainly due to term 1 as shown in figure 26(*a*). Note that the axial velocity gradient and turbulence levels are high near the nose of the ring (figures 13*b* and 23). Production due to shear as represented by the term 2 is mainly responsible for the high turbulence levels in the shear layers and on the edges of the ring (figure 26*b*). Regions of negative production (Glezer & Coles 1990) are also seen near the vortex ring cores, especially for $x/d < 5$, when the ring displays distinct cores. Contours of the term 3 shown in figure 26(*c*) suggest that the production is dominant only near the vortex cores. It is important to note that some of the random turbulence may be due to the phase jitter, which also may contribute to turbulence production. The uncertainty due to jitter is less than 2.8 % in the phase-averaged mean velocity, while the uncertainty in the normalized TKE production which is proportional to the cube of velocity standard deviation (Goodman 1960) is $\pm 3 \times 10^{-4}$.

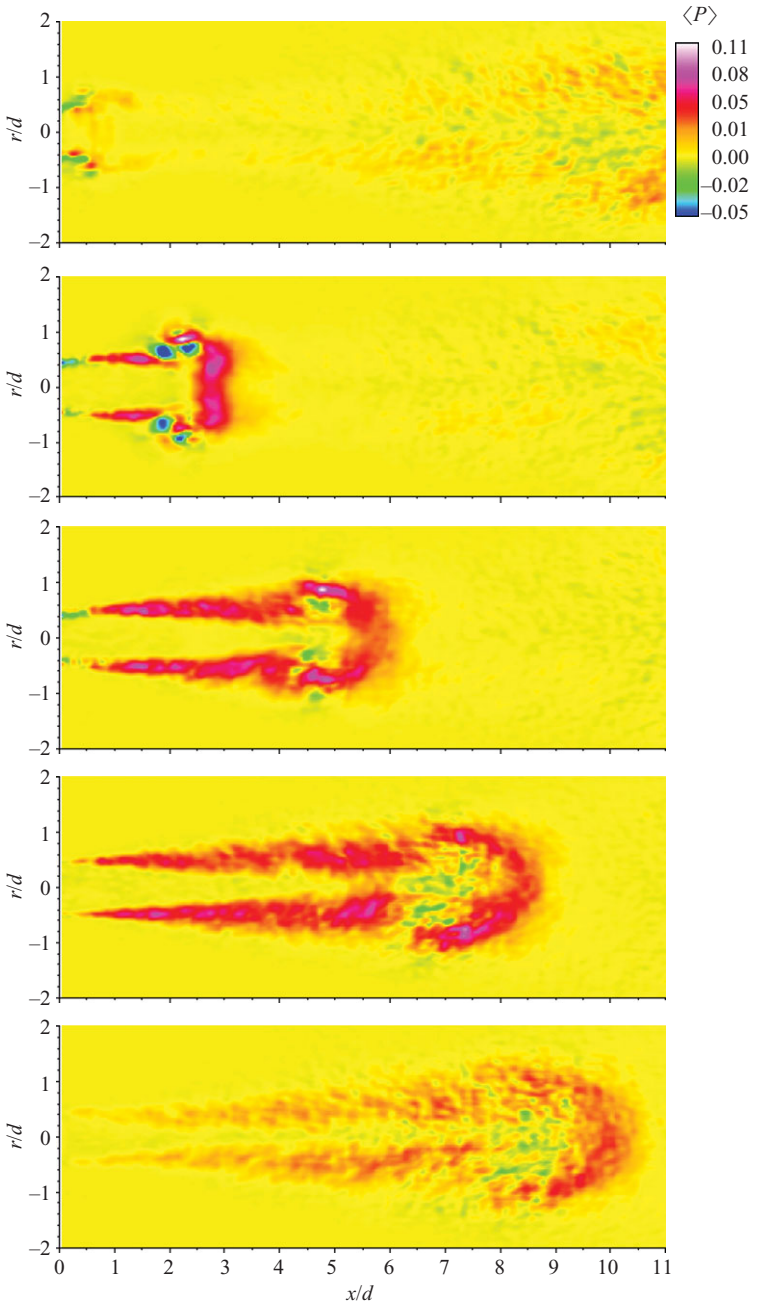

FIGURE 25. Production of phase-averaged random component of turbulent kinetic energy at different phases corresponding to figure 23.

3.4. *Global characteristics*

In this section, we look at several globally averaged mean properties, such as spread rate, entrainment, profiles of mean and fluctuating velocities, of the pulsed jet. What is of interest is how St or T^* affect these properties and how they compare with the

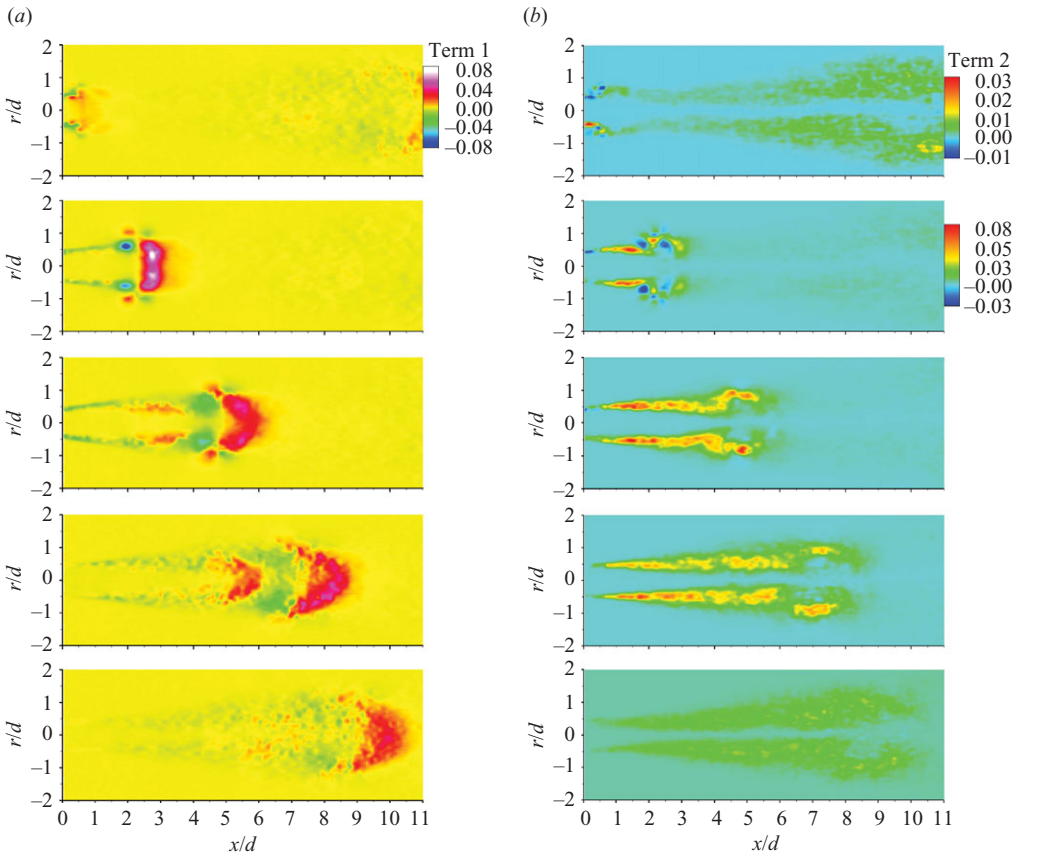

FIGURE 26. For legend see next page.

properties of a steady turbulent jet. As we shall see, many of the observed features are explained by dynamics that we discussed above. In all the figures, data corresponding to the steady jet are shown as a solid line. The effective origin of the steady jet obtained by linear extrapolation of the shear layer width is $-0.25d$.

Figures 27 and 28 respectively show the variations of the centreline axial velocity and the jet half-width with x/d for the pulsed jet and the steady jet. As seen in figure 27, the rate of centreline velocity decay increases with increase in Strouhal number. Correspondingly, the jet spreading rate also increases with Strouhal number as seen in figure 28. There is a sudden increase in the spread rate at some x/d, the value of which increases with reducing frequency. For example, the rapid increase for the $St = 0.11$ jet is noticed at $x/d \approx 4.5$, and for the $St = 0.03$ jet, it is at $x/d \approx 6.5$. This increase in spread rate is related to more mixing and entrainment which, in turn, depends on the distance between adjacent vortex rings and their strengths. A similar trend was also observed by Krueger & Gharib (2005). Remarkably, the lowest frequency jet, $St = 0.03$, shows characteristics similar to the steady jet as far as centreline velocity decay and spread rates are concerned.

With increase in frequency, the increased centreline velocity decay and increased spreading discussed above are also depicted qualitatively in mean axial velocity contours shown in figure 29, for the steady and $St = 0.06$ jets. It is to be remembered that the global average picture of a pulsed jet is the sum of the contributions from

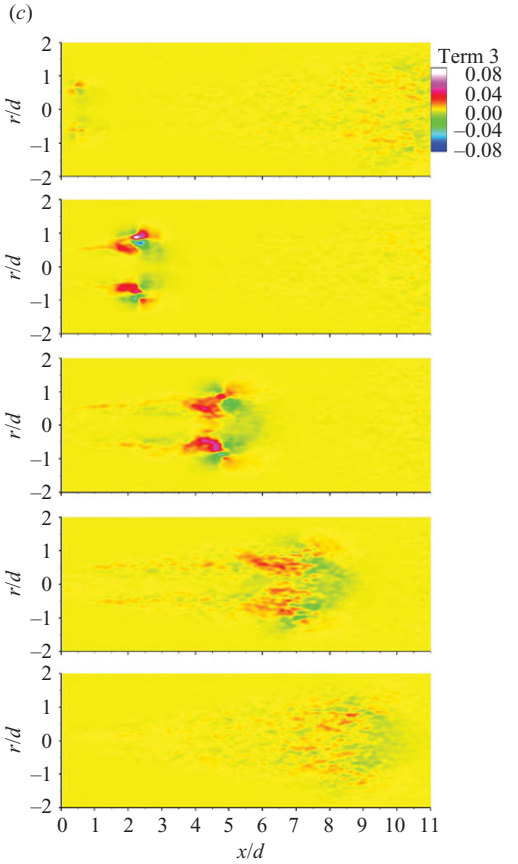

FIGURE 26. Contribution of different terms to turbulent kinetic energy production shown in figure 25; (*a*) $\langle u''u''\rangle \frac{\partial\langle u\rangle}{\partial x}$; (*b*) $\langle u''v''\rangle(\frac{\partial\langle u\rangle}{\partial r} + \frac{\partial\langle v\rangle}{\partial x})$; (*c*) Contribution of $\langle v''v''\rangle \frac{\partial\langle v\rangle}{\partial r}$.

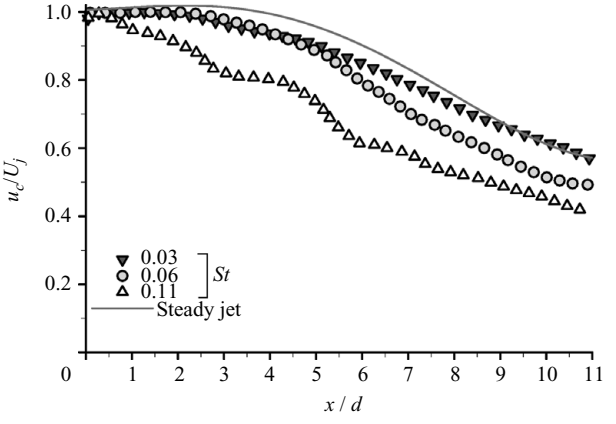

FIGURE 27. Global mean centreline velocity variation with downstream distance.

the ring, trailing jet and background jet. Consistent with the centreline velocity decay, the extent of the 'potential core' region of the pulsed jet decreases with increasing pulse frequency.

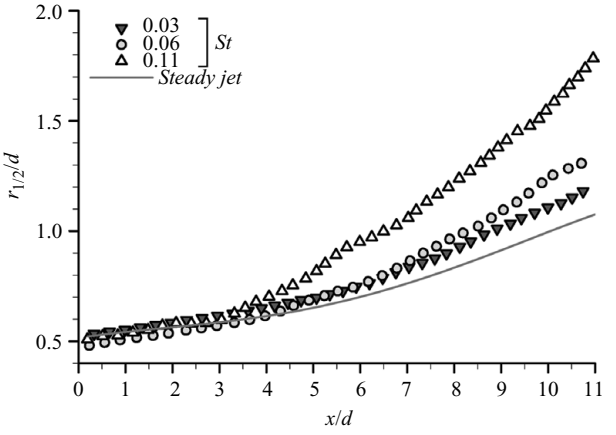

FIGURE 28. Global mean axial velocity half-width variation with downstream distance.

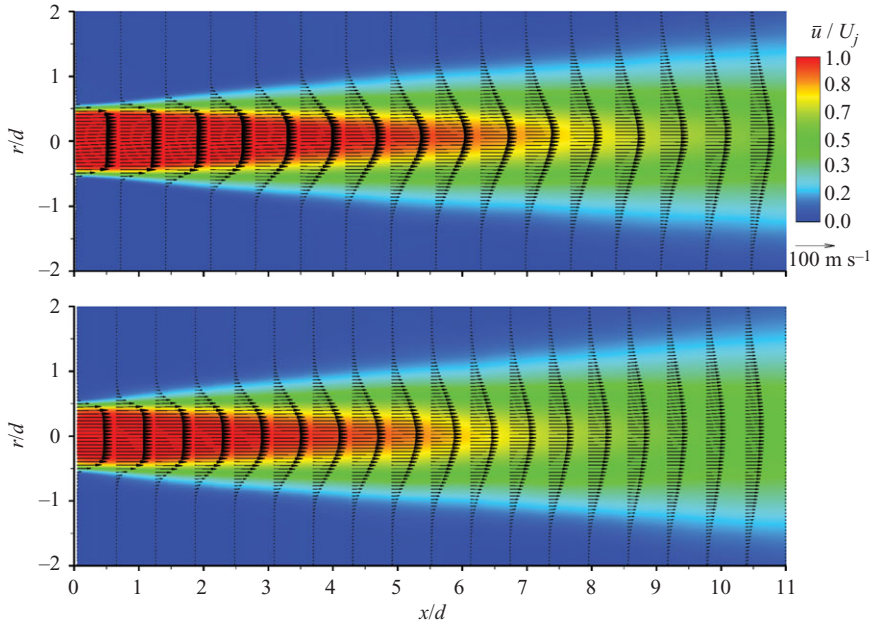

FIGURE 29. Contours of axial global mean velocity: (*a*) steady jet; (*b*) $St = 0.06$.

Figure 30 shows the normalized mass flow rates versus x/d for the pulsed jets and the steady jet. The mass flow rate is calculated as $\dot{m} = 2\pi\rho \int_0^{R_0} u(r) r \, \mathrm{d}r$, where R_0 is taken as the distance from the centreline of the jet to the top and bottom boundaries of the flow field under consideration. In these calculations, the total mass flow rate which includes the jet mass flow rate and the entrained mass flow rate at any given location is calculated for the cases under consideration. Beyond a certain x/d, the value depending on St, the entrainment rate of a pulsed jet is constant and same as that of a steady jet. It is important to note that due to the limited view of the PIV images in the radial direction, especially for the $St = 0.11$ case, the mass flow rate data for $x/d > 7$ may be underestimated. At $x/d = 10$, for $St = 0.11$ the mass flow rate is nearly twice the steady jet value. The variation of mass flow rate at $x/d = 10$, along

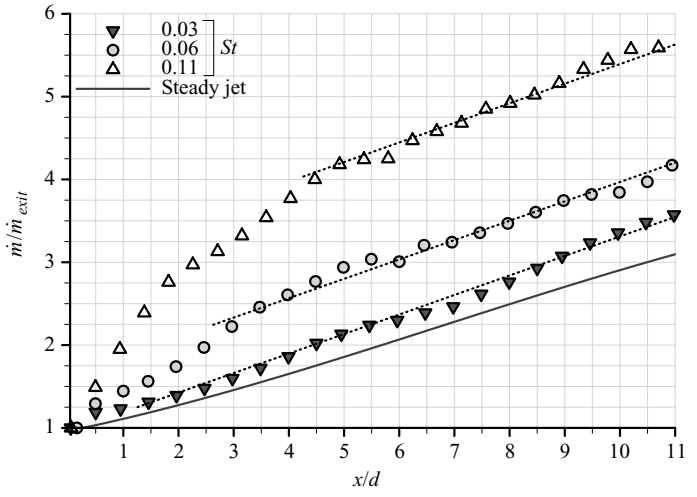

FIGURE 30. Variation of the normalized mass flow rate with downstream distance for different St.

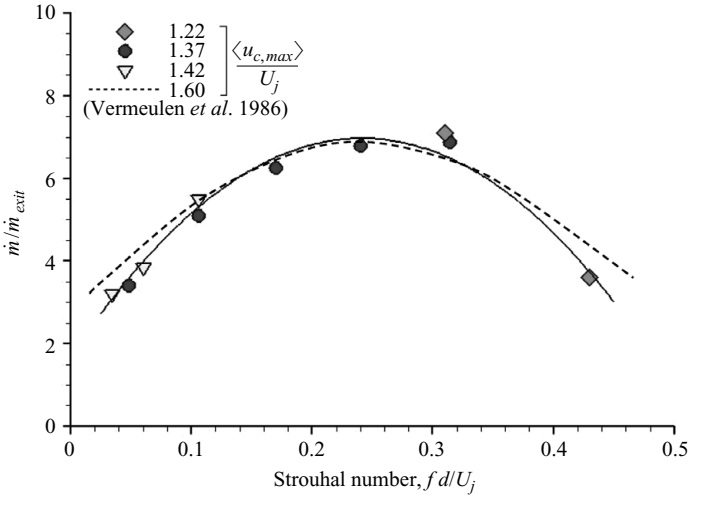

FIGURE 31. Variation of the normalized mass flow rate with St measured at $x/d = 10$.

with other Strouhal numbers considered in Choutapalli (2006), is shown in figure 31. Also included in the figure are the data taken from Vermeulen *et al.* (1986) where the r.m.s. values of pulsation amplitudes are nearly equal to those in the current study. It is apparent from these figures that a pulsed jet has a higher entrainment compared to a steady jet, with the maximum obtained at $St = 0.24$.

It is well known that entrainment is enhanced by perturbing a jet, which is tied in with formation of large structures (vortex rings) resulting from the perturbation (Crow & Champagne 1971; Hussain 1983). The enhanced entrainment is most likely due to the distinct vortex rings found in a pulsed jet. Most of the entrainment in a ring happens during the formation process (Dabiri & Gharib 2004), and the amount of entrainment depends in some way on the circulation and size of the ring. At the lowest frequency ($St = 0.03$), though the entrainment per ring is high, the rings are

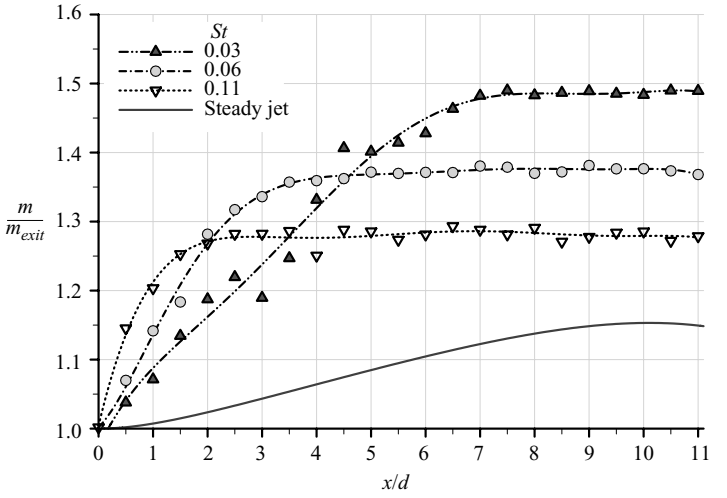

FIGURE 32. For legend see page no 57.

spaced so far apart that the overall entrainment is only marginally more than the steady jet value. With increasing frequency, it has been observed by Choutapalli (2006) that the rings become more closely packed, and as seen in figure 31 the entrainment increases up to St of about 0.24. The drop in entrainment after this value of St is because the rings were observed to be too close to each other (Choutapalli 2006) and the circulation per ring also decreased (figure 17). At the higher frequency, rings die sooner and along with them their entrainment capacity. It suggests that the entrainment is dependant on the strength and spacing of the vortex rings in a given flow field. The optimum combination of spacing and strength seems to be obtained at $St = 0.24$.

One main application of pulsed jets is in propulsion, that is, for producing thrust (e.g. pulse detonation engines and aquatic propulsion). As discussed in § 2.2, for a given exit mass flux, both momentum flux and energy flux at the exit are higher for a pulsed jet than for a steady jet. The axial momentum flux $M(x)$ is calculated, as outlined by Bremhorst & Harch (1979), by considering the following equation across the jet cross-section:

$$\frac{\partial}{\partial x}\int_0^{R_{0.01}} \frac{1}{\tau}\int_0^{\tau} (\langle u\rangle^2 + u'^2 + v'^2)\,\mathrm{d}t\,(r\,\mathrm{d}r) - 2\frac{\partial}{\partial x}\int_0^{R_{0.01}} \frac{1}{\tau}\int_0^{\tau} (v'^2)\,\mathrm{d}t\,(r\,\mathrm{d}r) = -\frac{R_{0.01}^2}{2\rho}\frac{\partial P_\infty}{\partial x}. \tag{3.1}$$

Here, $R_{0.01}$ is the radial location where the mean axial velocity is 1 % of that on the jet axis, u' and v' are the total fluctuating components as defined in § 2.2, P_∞ is the static pressure at the edge of the jet relative to the far field ambient pressure and ρ is the fluid density. The momentum flux is calculated by considering both terms on the left-hand side of (3.1) and is normalized with the exit value. The velocity fluctuations due to both the axial and radial components are taken into consideration since the pulsed jet flow field is dominated by coherent vortical structures in the initial few diameters. Figure 32(b) and (c) shows that the normal stress contribution due to both the axial and radial component of velocities at $St = 0.06$ is significant up to around $5d$.

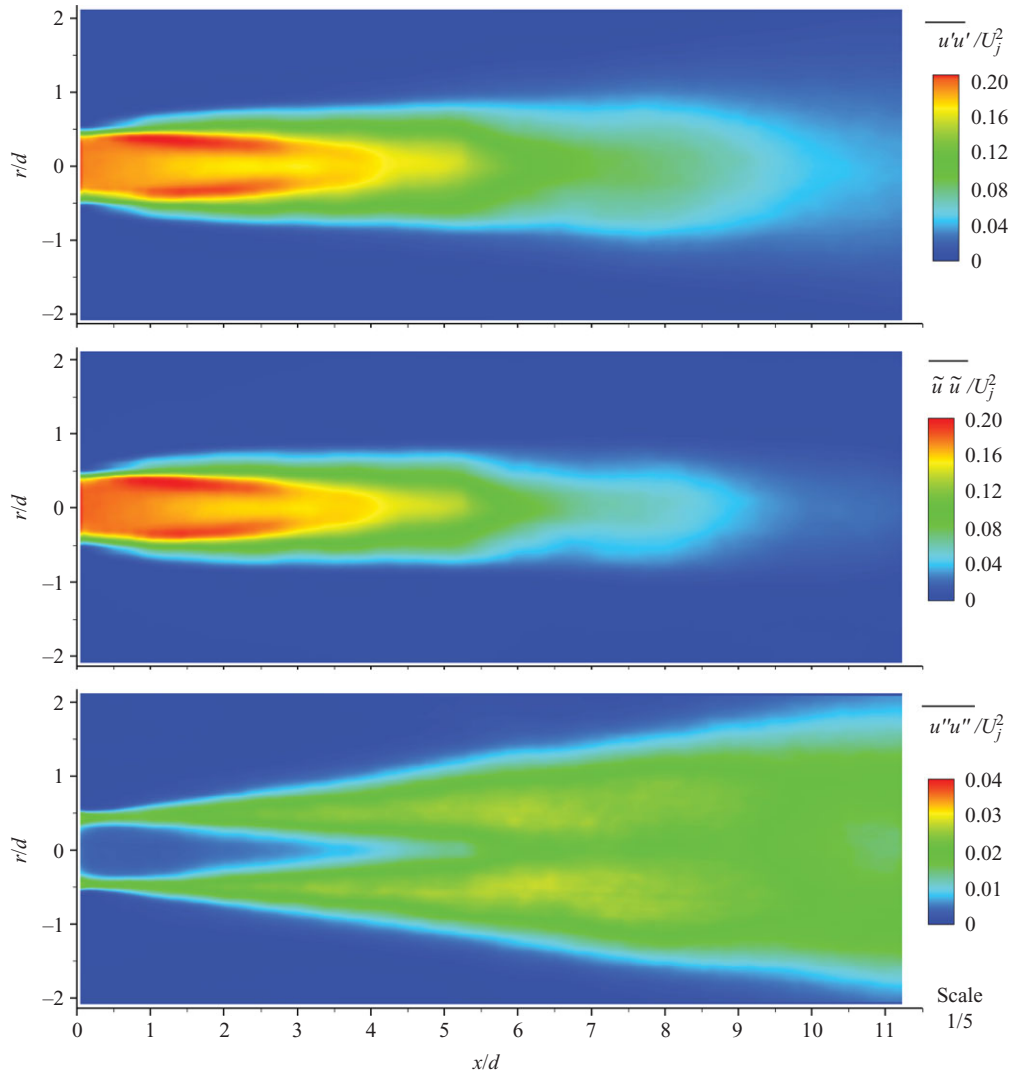

FIGURE 32. For legend see facing page.

Figure 32(*a*) shows the variation of the normalized momentum flux with downstream distance. It is seen that constancy of momentum is achieved around $7d$, $5d$ and $2d$ for $St = 0.03$, 0.06 and 0.11, respectively. A similar trend was also observed in the study of Bremhorst & Harch (1979). The results show that momentum constancy begins at nearly the same location where the vortex rings start to diffuse (see figure 17). Once the vortex rings begin to diffuse, the jet development is quite similar to that of a steady jet. In a steady jet, there is an increase of about 10 % in the momentum flux, which is attributed to the negative mean static pressure in the turbulent regions of the jet (Miller & Comings 1957; Hussain & Clark 1977). For the pulsed jet, there is a further increase of about 40 % for $St = 0.03$ over the steady jet. Law of conservation of momentum applied to a control volume starting at the exit and ending at a sufficiently downstream (say $x/d = 10$) station, where the pressure is nearly ambient, will show that the only way momentum flux can increase with

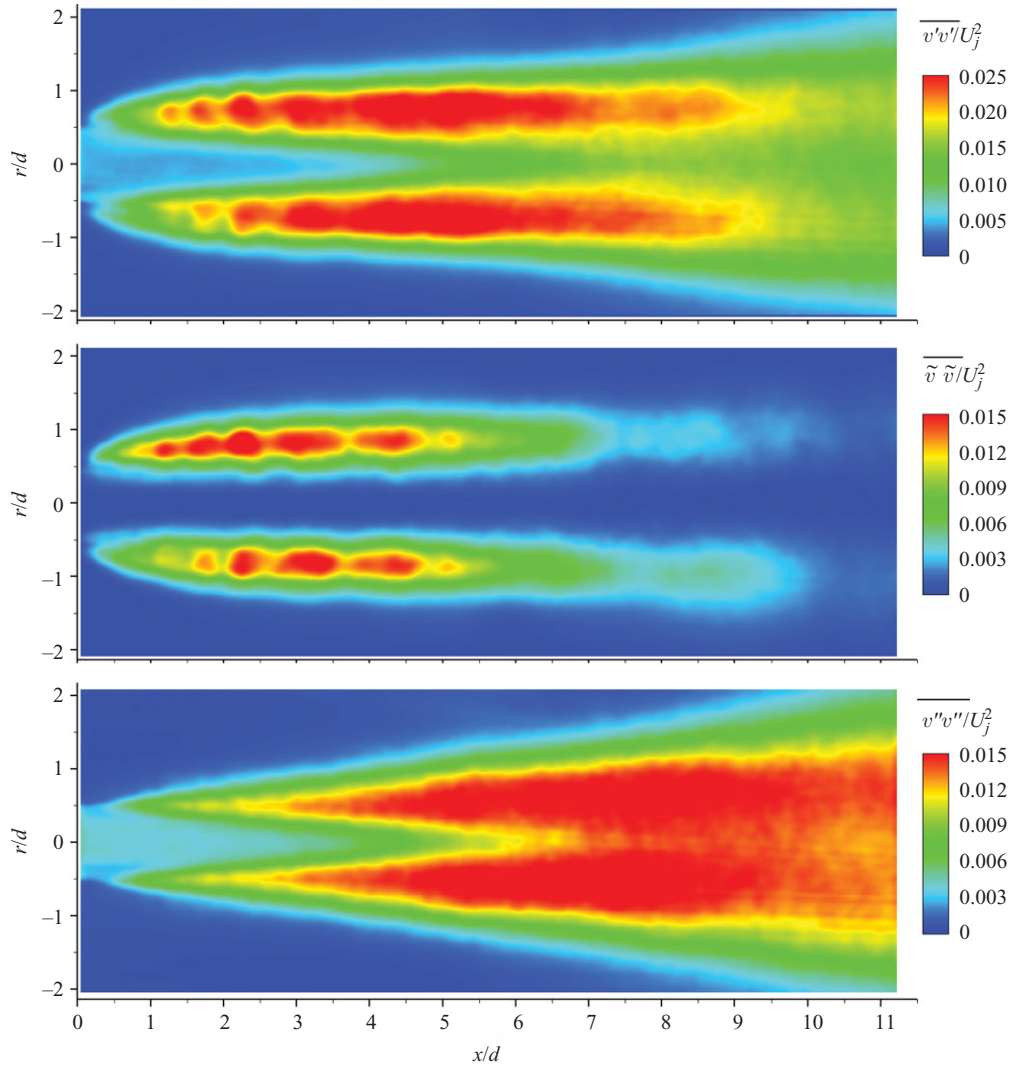

FIGURE 32. (*a*) Normalized momentum flux variation with downstream distance, (*b*) Contours of global mean axial normal stresses, (*c*) contours of global mean radial normal stresses for $St = 0.06$.

distance downstream is if the pressure at the exit exceeds the ambient value at least at some time during the cycle. The existence of this overpressure has been discussed by Krueger (2005) and is caused by an added mass effect of the jet fluid having to push and provide momentum to the stationary, or as in our case the slower moving background jet, fluid in front. The overpressure will occur only when the exit velocity is increasing with time, and should be roughly proportional to the time derivative of the exit velocity.

The global mean axial velocity profiles at selected locations downstream of the nozzle exit are shown in figure 33 for all the cases studied. Also included here are the data for a steady jet. It is to be remembered that the global average picture of a pulsed jet is the sum of the contributions from the ring, trailing jet and background

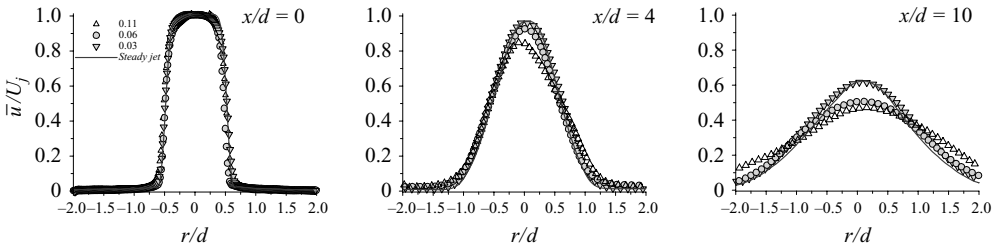

FIGURE 33. Global mean axial velocity profiles at three different downstream locations.

jet. The nearly top-hat profile at the nozzle exit transforms into a typical Gaussian profile at $x/d = 10$ with its shape being similar for pulsed and steady jets. The rapid spreading of the pulsed jet manifests itself into wider profiles with the peak velocity magnitudes being lowest for the $St = 0.06$ and $St = 0.11$ cases.

The variation of the centreline axial and radial turbulence (random component) intensity is shown in figure 34 for pulsed and steady jets. The steady jet turbulence intensity reaches a peak value of about 0.13 at $x/d = 7.5$. The $St = 0.11$ jet has the highest fluctuation levels, and the $St = 0.03$ and 0.06 jets reach nearly the same fluctuation levels as the 0.11 case around $x/d = 10$, indicating that characteristic of the jets is approaching that of a steady jet. The r.m.s. profiles of the axial velocity at selected downstream locations are shown in figure 35. The profile shapes are similar to that of the steady jet.

3.5. *Vortex ring characteristics*

As discussed in § 3.1, the main difference between the vortex rings produced in the present pulsed jets and the conventional ring is that in the pulsed jet case, the ring formation is in the presence of a background jet flow having a non-zero axial velocity and non-zero turbulence levels. It is interesting in these circumstances to look at the ring characteristics, such as the circulation development with time and the formation number (Gharib *et al.* 1998). The vortex ring is identified using the λ_2 criterion proposed by Jeong & Hussain (1995). To verify the value of ring circulation obtained by this method, the ring contour was also identified from the PIV data using the lowest detectable contour of $1\,\mathrm{s}^{-1}$ (Gharib *et al.* 1998). From both the methods, the maximum variation of the magnitudes of normalized ring circulation from each other was within 2 %. Hence, there was no significant difference in the ring circulation determined by the two methods. Normalized ring circulation is plotted against normalized slug length L in figure 36 for the $St = 0.06$ jet; $\overline{U}_e$ multiplied by time gives the 'length' of fluid that has issued out of the nozzle from $t = 0$.

The circulation increases during the ring formation, reaches a maximum at around the time ring separates from the trailing jet and then starts decaying. Figure 36 also shows the vorticity contour plots at selected times to bring out the correspondence between circulation and state of the ring. Figure 37 shows the ring circulation and the total (ring + trailing jet) circulation versus slug length. Extrapolating back from the maximum ring circulation point to intersect the total circulation curve gives the formation number to be about 3. This value may be compared with that obtained in a laminar piston-driven ring of 4 (Gharib *et al.* 1998) and a ring that is produced from open-ended shock tube of about 2.5 (Arakeri *et al.* 2004). Similarly, calculated formation number for $St = 0.03$ jet is around 4.5 and for $St = 0.11$ jet it is 2.5

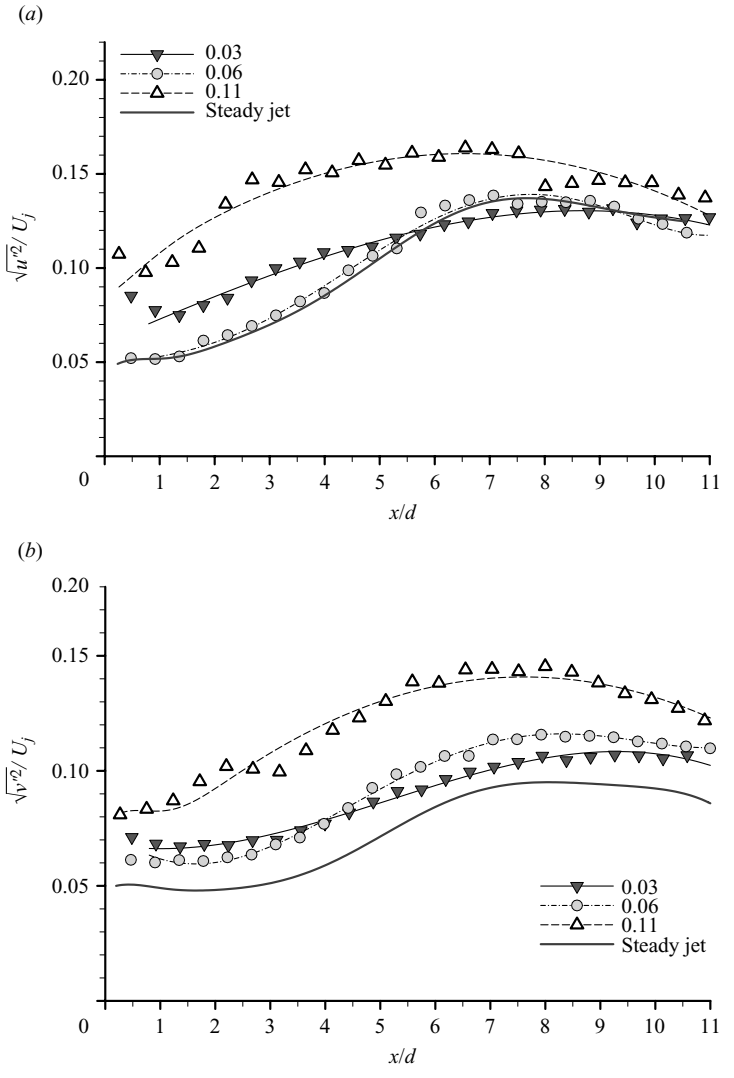

FIGURE 34. Variation of random component of the turbulent intensities along the centreline of the jet. (*a*) axial velocity; (*b*) transverse velocity.

(Choutapalli 2006). A potential cause of the difference in the formation number between the present experiments and those of Gharib *et al.* (1998) is the difference in the temporal variation of the velocity profile at the nozzle exit.

4. Summary and conclusions

A pulsed jet in the near field is perhaps best described as a series of vortex rings interspersed by jet-like flows. Many important global characteristics of a pulsed jet, such as entrainment and spreading rate, are determined by two main parameters: the spacing and strength of these vortex rings. The maximum circulation in the ring is proportional to the fluid slug length (L_r), which forms the ring, times an average exit velocity $\overline{U}_e L_r$. Here, L_r is equal to either L, the total slug length, or

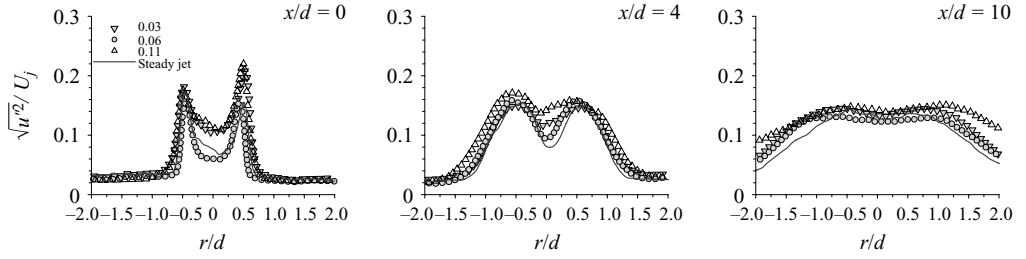

FIGURE 35. Profiles of the random turbulence intensity of the axial component at three different downstream locations.

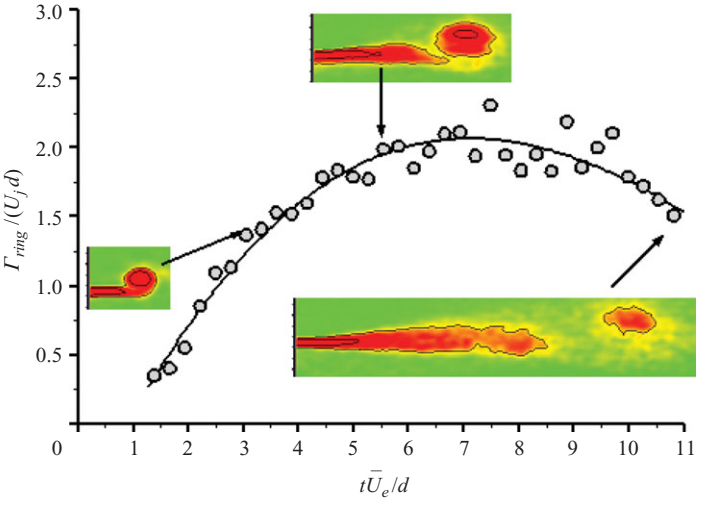

FIGURE 36. Evolution of the ring circulation at $St = 0.06$. Also shown are the vorticity contours at selected times.

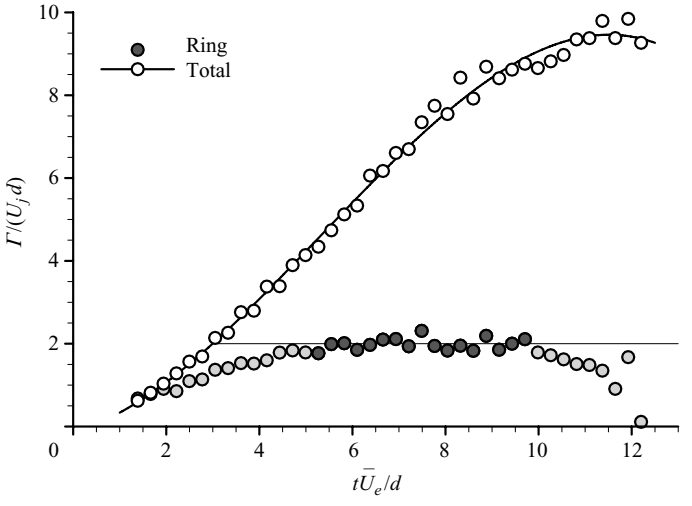

FIGURE 37. Evolution of total and ring circulations at $St = 0.06$.

some L_{max}, where $L_{max} \approx 3 - 4d$, which is determined by the maximum circulation the ring can incorporate. In the present experiments, the circulation reached close to the maximum possible for the three frequencies ($St = 0.03$, 0.06 and 0.11) and some of the circulation is absorbed into the trailing jet. Compared to a steady jet, pulsed jets entrain more fluid, spread faster and have higher momentum and energy fluxes. Maximum entrainment and spread rates can be expected to be achieved when vortex rings are as closely spaced as possible and, at the same time, have the maximum values of circulation.

There are two reasons why a pulsed jet has a higher momentum compared to that of a steady jet with the same mass flow rate. One reason is that any unsteadiness or pulsing at the exit increases the momentum flux at the exit, as given in table 1; this increase depends just on the profile of the exit velocity variation with time. The second reason for the increased momentum (figure 32) is the overpressure at the nozzle exit caused by an added mass effect of momentum being added to the ambient fluid when the jet fluid velocity is increasing with time (Krueger 2005). Both of these components responsible for the increase in momentum also contribute to a higher energy required to produce a pulsed jet.

The evolution of a low-frequency jet depends on the individual evolutions of the three components – vortex ring, background and trailing jets – and on the interactions among these three components. Taking the example of the $St = 0.06$ jet, we discussed some properties of these three components. Various axial gradient terms, for example, $\partial\langle u''u''\rangle/\partial x$, $\langle u\rangle\partial\langle u'u'\rangle/\partial x$, occurring in the axial momentum and turbulence energy equations, and normally neglected under the boundary layer assumption, are likely to be important in calculating the pulsed jet evolution (Bremhorst & Gehrke 2000). It appears that vortex ring in a pulsed jet decays more rapidly than an individual turbulent ring (Maxworthy 1974, 1977; Glezer & Coles 1990). This more rapid decay is related to interactions with the jets upstream and downstream of the ring. Bremhorst & Gehrke (2000) give detailed measurements of turbulence quantities in the far field (x/d around 50) of their very low St ($= 0.0035$) jet, and also comment on the importance of extra terms due to unsteadiness and axial gradients for modelling of the turbulence in a pulsed jet.

It is not known how far downstream vortex rings exist as distinct entities, but what is known is that low-frequency pulsed jets show modulation in time at large x/d. For example, for the $St = 0.0035$ pulsed jet, a modulation in axial velocity of about 40 % of the local average centreline velocity was observed at $x/d = 70$ (Bremhorst & Gehrke 2000). We can obtain an estimate of the downstream distance at which a pulsed jet will transition to a steady one. The convection velocity of the ring, or of the nose of the pulsed jet (in the absence of a ring), is expected to reduce with downstream distance, say as x^{-n}. Then $\Delta x_{ring} \sim \tau x^{-n}$ will correspondingly reduce and the rings will bunch closer together with downstream distance. At the same time, the width of the ring ($b = r_{1/2}$) will increase with distance, $b \sim x^m$. We may consider the pulsed jet to become steady when the 'rings' are close enough $\Delta x_{ring} = b$, which gives $x_{transition} \sim \tau^{-(m+n)}$, where $x_{transition}$ is the distance at which the pulsed jet transitions into a steady jet.

We would like to thank Dr Mehmet B. Alkislar, who has worked on this project during the design and development phase of the facility. He was also largely responsible for the implementation of PIV. The work was funded by DARPA under the technical supervision of Mr Sam Wilson.

REFERENCES

Alkislar, M. B. 2001 Flow field measurements in a screeching rectangular jet. PhD dissertation. Florida State University, Tallahassee.

Alkislar, M. B., Choutapalli, I., Krothapalli, A. & Lourenco, L. M. 2005 Flow field of a pulsed jet: a PIV study. *AIAA Paper* 2005-1274.

Alkislar, M. B., Krothapalli, A. & Lourenco, L. M. 2003 Structure of a screeching rectangular jet: a stereoscopic PIV study. *J. Fluid Mech.* **489**, 121–154.

Arakeri, J., Das, D., Krothapalli, A. & Lourenco, L. 2004 Vortex ring formation at the open end of a shock tube: a particle image velocimetry study. *Phys. Fluids* **16** (4), 311–331.

Bremhorst, K. & Gehrke, P. J. 2000 Measured Reynolds stress distributions and energy budgets of a fully pulsed round air jet. *Exp. Fluids* **28**, 519–531.

Bremhorst, K. & Harch, W. H. 1979 Near field velocity measurements in a fully pulsed subsonic air jet. In *Proceedings of the First Symposium on Turbulent Shear Flows* (ed. F. Durst, et al); *Turbulent Shear Flows,* pp. 37–54. Springer.

Bremhorst, K. & Hollis, P. G. 1990 Velocity field of an axisymmetric pulsed, subsonic air jet. *AIAA J.* **28**, 2043–2049.

Cantwell, B. J. & Coles, D. 1983 An experimental study of entrainment and transport in the turbulent near wake of a circular cylinder. *J. Fluid Mech.* **136**, 321–374.

Choutapalli, I. M. 2006 An experimental study of a pulsed jet ejector. PhD thesis, Florida State University, Tallahassee.

Choutapalli, I. M. & Krothapalli, A. 2009 Pulse jet ejector thrust augumentor characteristics. *J. Propulsion Power*, submitted.

Crow, S. & Champagne, F. 1971 Orderly structure in jet turbulence. *J. Fluid Mech.* **48**, 547–591.

Dabiri, J. O. 2005 On the estimation of swimming and flying forces from wake measurements. *J. Exp. Biol.* **208**, 3519–3532.

Dabiri, J. O. & Gharib, M. 2004 Fluid entrainment by isolated vortex rings. *J. Fluid Mech.* **511**, 311–331.

Gharib, M., Rambod, E., Kheradvar, A., Sahn, D. J. & Dabiri, J. O. 2006 Optimal vortex formation as an index of cardiac health. *Proc. Nat. Acad. Sci.* **103**, 6305–6308.

Gharib, M., Rambod, E. & Shariff, K. 1998 A universal time scale for vortex ring formation. *J. Fluid Mech.* **360**, 121–140.

Glezer, A. & Coles, D. 1990 An experimental study of a turbulent vortex ring. *J. Fluid Mech.* **221**, 143–183.

Goodman, L. A. 1960 On the exact variance of products. *J. Am. Statist. Assoc.* **55**, 708–713.

Hussain, A. K. M. F. 1983 Coherent structures: reality and myth. *Phys. Fluids* **26**, 2816–2850.

Hussain, A. K. M. F. & Clark, A. R. 1977 Upstream influence on the near field of a plane turbulent jet. *Phys. Fluids* **20**, 1416–1427.

Jeong, J. & Hussain, F. 1995 On the identification of a vortex. *J. Fluid Mech.* **285**, 69–94.

Johari, H. 2006 Scaling of fully Pulsed jets in cross flow. *AIAA J.* **44**, 2719–2725.

Krueger, P. S. 2005 An overpressure correction to the slug model for vortex ring circulation. *J. Fluid Mech.* **545**, 427–443.

Krueger, P. S. & Gahrib, M. 2005 Thrust augmentation and vortex ring evolution in a fully pulsed jet. *AIAA J.* **43** (4), 792–801.

Lourenco, L. M. & Krothapalli, A. 2000 True resolution PIV: a mesh-free second-order accurate algorithm. In *Proceedings of the Tenth International Symposium on Applications of Laser Techniques in Fluid Mechanics.* Lisbon, Portugal.

M'Closkey, R. T., King, J., Cortelezzi, L. & Karagozian, A. R. 2002 The actively controlled jet in crossflow. *J. Fluid Mech.* **452**, 325–335.

Manganiello, E. J., Valerino, M. F. & Essig, R. H. 1945 Sea-level performance tests of a 22-inch diameter pulse-jet. *NACA Memorandum*, Report E5J02.

Maxworthy, T. 1974 Turbulent vortex rings. *J. Fluid Mech.* **64**, 227–239.

Maxworthy, T. 1977 Some experimental studies of vortex rings. *J. Fluid Mech.* **81**, 465–495.

Mei, R. 1996 Velocity fidelity of flow tracer particles. *Exp. Fluids* **22**, 1–13.

Miller, D. & Comings, E. 1957 Static pressure distribution in the free turbulent jet. *J. Fluid Mech.* **3**, 1–16.

Mohseni, K., Ran, H. & Colonius, T. 2001 Numerical experiments on vortex ring formation. *J. Fluid Mech.* **430**, 267–282.

Reynolds, W. C. & Hussain, A. K. M. F. 1972 The mechanics of an organized wave in turbulent shear flow. Part 3. Theoretical models and comparisons with experiments. *J. Fluid Mech.* **54**, 263–288.

Rosenfeld, M., Rambod, E. & Gharib, M. 1998 Circulation and formation number of laminar vortex rings. *J. Fluid Mech.* **376**, 297–318.

Schuster, J. M. & Smith, D. R. 2007 An experimental study of the formation and scaling of a round synthetic jet. *Phys. Fluids* **19** (4).

Siekmann, J. 1963 On the pulsating jet from the end of a tube, with application to the propulsion of certain aquatic animals. *J. Fluid Mech.* **15**, 399–318.

Shariff, K. & Leonard, A. 1992 Vortex rings. *Ann. Rev. Fluid Mech.* **24**, 235.

Smith, B. L. & Glezer. A. 1998 The formation and evolution of synthetic jets. *Phys. Fluids* **10** (9), 2281–2297.

Vermeulen, P. J., Ramesh, V. & Wai, K. Y. 1986 Measurements of entrainment by acoustically pulsed axisymmetric air jets. *J. Engng Gas Turbines Power* **108** (3), 479–484.

Weihs, D. 1977 Periodic jet propulsion of aquatic creatures. *Fortschr. Zool.* **24**, 171–175.